LUNDS UNIVERSITET
Naturvetenskapliga fakulteten

Master's Thesis Project

Project Duration of 8 Months
Spring 2023-Autumn 2023

Division of Particle and Nuclear Physics
Department of Physics

Detector Pixel

EVR

$\alpha_a \ (\gamma_a)$

$\alpha_b \ (\gamma_b)$

Decay Chains of Fast Alpha Emitters in the Actinide Region

$\alpha_c \ (\gamma_c)$

Author
Tanvir Sayed

$\alpha_d \ (\gamma_d)$

Supervisor
Luis Sarmiento Pico

Examination
January 19, 2024

Abstract

With the advent of increasingly advanced spectroscopic instruments after the turn of the century, it has become accessible to unravel the structure of instantly 'vanishing' nuclei, with lifetimes as short as $1\,\mu s$, and responsible for pile-up events in analog electronics. Experimental data has been recorded by the Nuclear Structure Group at Lund University for ^{48}Ca/^{50}Ti + $^{nat.}$Hf reactions during the preparation stages of the 'Spectroscopy along Decay Chains of Element 114, Flerovium' which was carried out in two subexperiments in 2019 and 2020 at the GSI Helmholtz Centre for Heavy Ion Research in Darmstadt, Germany. These reactions have yielded hints of spectroscopic information for fast α-decaying nuclei in anticipated long α-decay chains in the actinide region. Many of these nuclei have not been studied in detail since their discovery decades earlier.

This work adds new indications which contribute to the nuclear structure information for some of these fast α emitters. The investigated region of the nuclidic chart is in the vicinity of heavy-, neutron-deficient isotopes normally considered a stepping stone for answering open questions of how approaching the $N = 126$ shell closure affects the nuclear structure of isotopes in this region. The recorded data was prepared to implement a decay-chain-hunting procedure. Comprehensive data analysis has been carried out to deduce the decay chains of the several, fast α emitters lying in the region of the neutron-deficient uranium isotopes. The most prevalent decay chain seen is that of the ^{225}U isotope of which all four α decays are observed and a decay scheme including α-decay fine structure has been produced. This acted as a proof-of-concept technique for further searches. More importantly, there are strong indications of possibly two new states as well as an improved half-life of ^{217}Ra. Some of the very fast α decays have been observed successfully. Lastly, indications of a handful of new excited levels have been found. Building on the work done in this project is expected to lead to exciting findings that would increase our knowledge and understanding of the nuclear structure of these fast α-decaying isotopes.

Acknowledgments

Contents

1 Introduction

Research in the field of nuclear physics has been growing to expand our knowledge and understanding of the nucleus and the plethora of phenomena related to it. Going forward from the study of naturally occurring and semi-stable nuclei in the past, the 'nuclear' scientists of the present day are exploring the structure of rare, exotic and new nuclei that are challenging to both produce and study. Such nuclear structure studies also include querying the limits of existence by discovering instantly vanishing, unstable nuclei and their properties; investigating potentially deformed nuclei which are present in the heavy end of the chart covering many not-defined nuclides; probing nuclear shells to study shell structure and nuclear magic numbers; or even striving to produce the most long-lived – if not simply naturally existing – superheavy isotope in the theorised 'island of stability'.

Alpha-decay spectroscopy – where one studies the α decays of a radioisotope or a chain of α decays is a very valuable technique used for nuclear structure studies and even more so in heavy and superheavy nuclei where α decays are predominant. Investigating α decays of radioactive nuclei allows us to follow its transition from unstable to relatively more stable configurations and deduce nuclear structure properties of the different nuclear states in both the initial and final nuclei. Alpha-decay spectroscopy is being used extensively in current research of superheavy elements on the quest to reach the island of stability and validate if $Z = 120$, a theory favourite, is indeed a magic number. It is also used in studies of very short-lived isotopes that had been discovered many decades ago but previously there was an absence of electronics and instruments that could keep up with the lifetimes of decay of the synthesised nuclei with lifetimes as short as $1\,\mu s$.

An important alpha-decay spectroscopy experiment is the U310 one 'Spectroscopy along Decay Chains of Element 114, Flerovium' that was carried out in two runs at the GSI Helmholtz Centre for Heavy Ion Research in Darmstadt, Germany. It was performed by the Nuclear Structure Group from Lund University and was primarily part of the doctoral studies work of Anton Såmark Roth. In the main experiment, a plutonium target wheel containing ^{242,244}Pu isotopes was bombarded with accelerated ^{48}Ca ions, and the resulting fusion-evaporation residues of flerovium were studied using the decay station `TASISpec+` behind the gas-filled separator `TASCA`. The experiment yielded many flerovium decay chains which included those for the even-even ^{288}Fl, ^{286}Fl isotopes, and the even-odd ^{289}Fl isotope. The most significant results retrieved from the decay chains were the discovery of the ^{280}Ds, the discovery of an excited state in ^{282}Cn, as well as the presence of fine structure in the ^{289}Fl α-decay chain. Furthermore, it was also seen that $Z = 114$ is not a magic number as was predicted by some models. Overall, it had laid an important checkpoint for further spectroscopic studies towards the aim of reaching heavier superheavy elements and in particular those in the island of stability [1].

During the preparation stages of the two experimental runs, data from reactions of ^{48}Ca and ^{50}Ti on a $^{nat.}$Hf target wheel were recorded during parasitic runs to investigate pile-up signals emerging from fast α emissions from the produced isotopes and further develop their analysis routine [1]. At the same time, the reactions are expected to yield valuable

spectroscopic information for many fast α-decaying nuclei along decay chains in the relevant actinide region. This formed the foundation for the Master's thesis project 'Decay Chains of Fast Alpha-Emitters in the Actinide Region', which is the topic of this report. The region of the nuclidic landscape that is of relevance in this thesis work is the neutron-deficient uranium isotopes in the actinide region, presented in Fig. 1. The fast α decays occur from unstable nuclei with lifetimes ranging in the milliseconds to fractions of a microsecond. The study of these α decays has become accessible only in recent decades with the advent of highly advanced spectroscopic instruments that allow high-resolution α-decay spectroscopy capable of picking out the fast α decays. Through this study during the scope of the degree project work, it is desired to achieve validation of existing decay schemes, devise a proof-of-concept technique to extract chains of α decays involving fast α emissions, and add further nuclear structure information for some of these fast α emitters. The investigated region of the nuclidic chart is in the vicinity of heavy, neutron-deficient isotopes and can aid in giving insights for future experiments exploring the $N = 126$ shell closure and how it affects the nuclear structure.
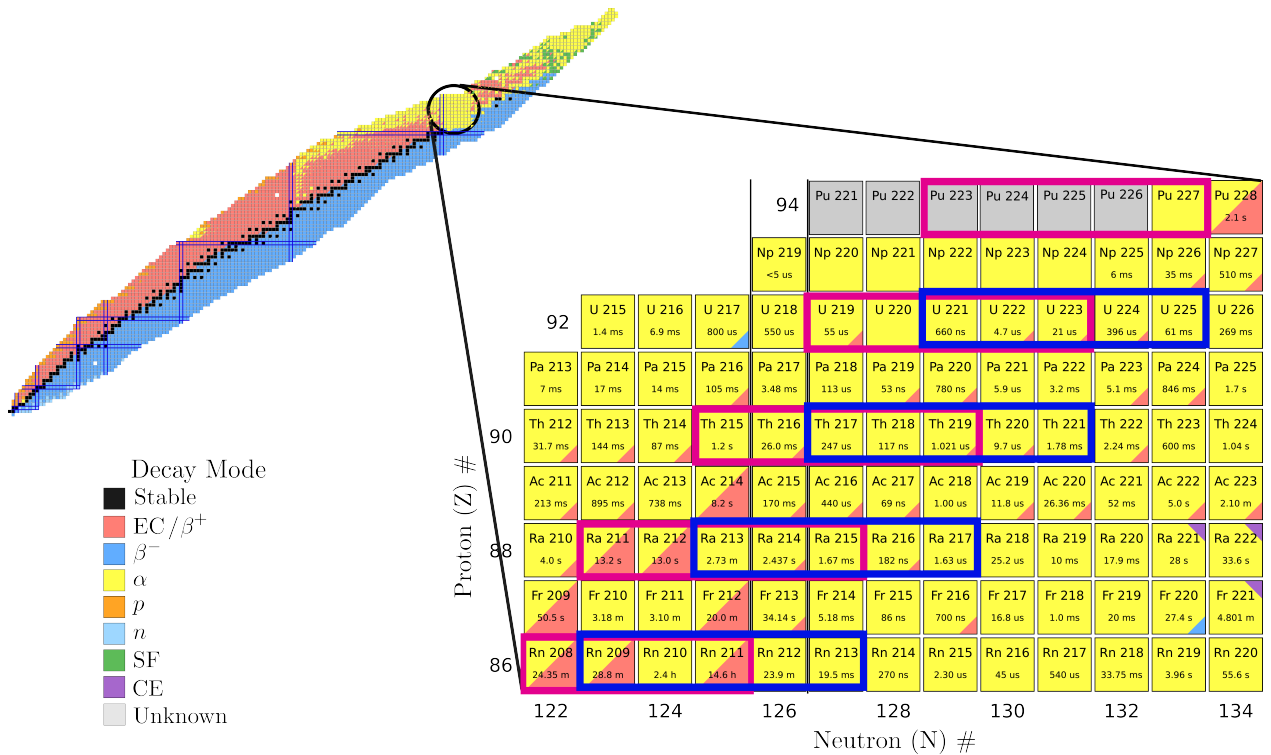
Figure 1: Portion of the nuclidic chart with the actinide region highlighted where the decay chains of the fast α emitters are expected. The relevant isotopes when using the ^{48}Ca beam are enclosed in blue rectangles while the relevant isotopes when using the ^{50}Ti beam are enclosed in magenta rectangles. Values of the half-lives given with the isotope are from nuclear datasheets [2].

Following the brief background and motivation of the study and its relevance in the field of nuclear structure research given in this introduction, the next section covers the key concepts including the theory of the nucleus, its properties as described by the shell model, and the main decay mode of interest in this work, the α decay, its properties as well as its connection

to nuclear structure. In the third section, the experimental setup and the data acquisition system that was used to retrieve the ^{48}Ca/^{50}Ti+ $^{\text{nat.}}$Hf reaction dataset for our analysis is detailed. This is succeeded by a section describing the entire data analysis carried out from the initial raw digitised preamplifier signals to the process of determining 'valid' α-decay chains following a chain hunt technique. Energy and time plots from the data analysis and the finalised decay schemes built from them are presented and discussed in the Results section. This included a decay scheme for the ^{225}U isotope using 'clean' decay chains with α emissions considered only in beam-off periods, as well as parts of one other decay scheme where the first α decay also came in beam-on periods but was able to be identified. Finally, the report is wrapped up with some concluding remarks and an outlook on future work and improvements in related research following this project.

2 Theory

2.1 The Nucleus, Nuclear Forces and Shell Model

Visible matter in the Universe is composed of building blocks known as the atom. An atom consists of a positively charged, mass-dense central part – named the nucleus – surrounded by a cloud of negatively charged electrons. While the electrons are responsible for the chemical properties of the atom, it is the nucleus that defines it. Nucleons, which are protons and neutrons, make up the atomic nucleus. The positively charged protons and electrically neutral neutrons have masses which are about 1800 times the electron mass. As a consequence, the nucleus carries more than 99.9 % of the total mass of the atom. The number of protons in the nucleus is referred to as the atomic number Z and this defines the chemical element that the atom belongs to. A specific element can still have several versions of nuclei which differ by the number of neutrons N, called isotopes where the total number of protons and neutrons, denoted the mass number A, is different [3].

The nucleons experience, between them, the nuclear force which is very repulsive at very short distance, attractive at short range (a couple femtometers) and soon after it goes to zero. The nuclear force is mediated between the nucleons via the exchange of virtual mesons (dominantly pions) acting as mediators, while the protons additionally exert a repulsive Coulomb force on each other mediated by their electromagnetic field. The nucleus is held together through the balance of the nuclear and Coulomb forces. The nuclear force is stronger than the Coulomb force but due to the repulsive nature at very short range, the nucleons are spread out evenly at an average distance rather than populated densely in a mass centre. The nuclear force is therefore dominant at short ranges with its nearest neighbours, while the Coulomb force has – in principle – infinite range. The number of protons Z and the number of neutrons N are comparable in stable, low-mass nuclei ($Z < 20$), whereas as the nucleus gets bigger with more and more nucleons, N requires to be higher in high-mass nuclei to counteract the stronger Coulomb forces brought about by higher Z. In the region of heavy isotopes, relevant to this thesis work, the $\frac{N}{Z}$ ratio is about 1.45. This $\frac{N}{Z}$ ratio is one factor that determines the stability of the nucleus and, generally, unstable nuclei decay in a physical phenomenon whereby the ratio is improved [4].

It has been noted that the total mass of all nucleons constituting the nucleus exceeds the actual, measured mass of the nucleus. This mass defect is the binding energy of the nucleus. The higher the binding energy per nucleon in a nucleus, the more stable its configuration. This quantity rises steeply when going from low Z elements reaching a maximum at around Fe before slowly falling.

The properties of the nucleus are determined and explained using models. One of the models that best describes the nucleus and explains several properties is the shell model. In this model, the nucleons in the nucleus occupy so-called shells and sub-shells of different energy regions, distinguished as quantized energy levels, that determine the overall nuclear structure and (energy) state. All the nucleons together themselves are responsible for the potential in which they are enclosed. The nucleons are fermions with a characteristic 'spin' of one-half. The projections of the spin, m_j, can be either $\frac{1}{2}$ or $-\frac{1}{2}$. The nucleus can be considered to have a nuclear potential that is filled with nucleons at quantized energy levels. The available energy states of the neutrons and protons are separate, i.e. the protons fill in states separate from the neutrons. According to Pauli's exclusion principle, only one unique particle can occupy any given state, i.e. no two particles can have the same quantum numbers [5]. Since, nucleons are half-spin fermions, two protons or neutrons of opposite spin projections can couple together to occupy a given energy state commonly called an orbital. In a stable, nuclear configuration, the nucleons fill up starting from the lowest energy state upwards. These energy states are quantized and the energy differences between successive states are comparable at some quantum numbers while it increases sharply at others. This allows us to group the nucleon occupancy into shells as well as subshells (with slightly smaller energy gaps relative to shells) and the nucleon numbers at which these steep jumps in energy are seen are referred to as magic numbers, analogous to the noble gases in atomic physics. Nuclei with magic number configuration are more stable relative to non-magic ones and hence an interesting region for nuclear structure investigations. It is speculated that there is an island of stability even at superheavy nuclei region ($Z > 103$) around the possible new Z magic number 120 [6, 7].

The properties of the nucleus are heavily impacted by the total angular momentum it has. This total angular momentum is usually simply called the spin. Since an orbital holds two nucleons of opposite spin, the spin in those adds up to zero. In the extreme single-particle shell model, only unpaired nucleons giving a net spin determine the most prominent observed characteristics. These unpaired nucleons typically occupy the outermost nuclear shell, the so-called valence shell. All the nucleons, paired and unpaired, in the valence shell are called valence nucleons. This simplification is quite accurate in light nuclei. However, at higher A, it becomes important to consider all the nucleons in the valence shell, not just the unpaired ones. For many nuclei, several or all nucleons together in the nucleus appear to have a significant contribution in a 'collective effect'. An example of this behaviour is as follows. The ground state of a nucleus, i.e. the lowest energy configuration, is the configuration when all the energy states are occupied from the lowest up in order resulting in a total spin of 0 or $\frac{1}{2}$. For any even-even nuclei, the ground state is almost always 0^+, where the + indicates the parity. The next excited state is when a nucleon pair is broken and occupies separate orbitals in a 2^+ nuclear state with an energy of about $2\,\text{MeV}$ corresponding to the energy of

breaking the pair. Yet, it has been experimentally observed that at least one isotope of the heavy elements has a 2^+ state with a much lower energy of about $1.2\,\mathrm{MeV}$, a consequence of the collective effect [8].

As mentioned earlier, the heavier the nucleus gets, the more the Coulomb force begins to overtake the nuclear force making the nucleus unstable and promoting particle emission. A nucleus can also have nucleons in higher energy orbitals while having empty lower ones forming so-called excited states. These unstable nuclei, commonly called radioactive nuclei, undergo radioactive decay by emitting one or more particles and releasing energy. This results in a new configuration of the nucleus which has lower energy but higher binding energy per nucleon. Radioactive decay involves the emission of ionising particles that can lead to the removal of electrons from atoms in matter on interaction, ionising the atom in the process. The main types of radioactive decay include α decay, γ decay, β decay, electron capture, and fission. Heavy nuclei with very high Z and N, such as those in the actinide region, can undergo several α decays in a decay chain to reduce Z and hence the Coulomb repulsion, eventually reaching a stable configuration with N and Z close to magic numbers. Alpha decays are an extremely valuable probe for exploring the properties of the nucleus and are common in decay spectroscopy experiments, especially for heavy and superheavy nuclei, such as the ones in this work. This makes it necessary to delve deeper into the alpha-decay process and the nuclear information that it contains. This more detailed discussion of α decays is given in the next subsection.

2.2   Alpha Decay
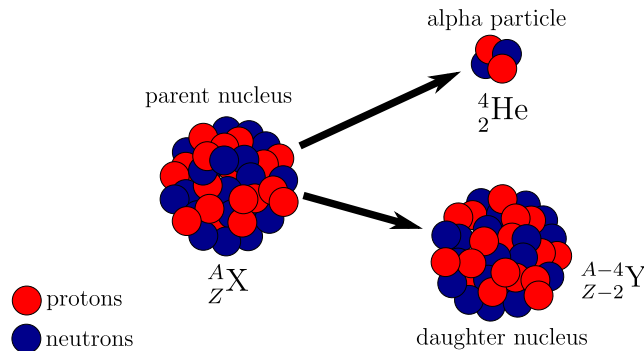
Figure 2: A parent nucleus with an excess of protons decays by emitting an α particle to form a daughter nucleus with lower binding energy. Red colour is used to depict the protons while blue colour to depict neutrons.

Alpha decay is a physical phenomenon whereby unstable nuclei with high Z transform into lower Z nuclei by emitting two protons and two neutrons in the form of a helium nucleus (as illustrated in Fig. 2). Alpha decay reduces the Coulomb repulsion between the protons when the attractive nuclear force between the nucleons is not able to balance out the repulsion. The Coulomb force increases with the square of Z and hence, in high Z nuclei – with $Z > 80$, such as the nuclei studied in this thesis work – alpha decays are the dominant decay process. An alpha decay of a parent nucleus X with mass number A, proton number Z, and neutron

number N undergoing α decay into a daughter nucleus Y can be represented in the form

$$^{A}_{Z}X_{N} \rightarrow ^{A-4}_{Z-2}Y_{N-2} + ^{4}_{2}He_{2}. \tag{1}$$

The mass of the system decreases in the process as it is transferred into the kinetic energy of the decay products. The energy change brought about by any reaction is called its Q-value, which is positive for a spontaneous process. Nuclei with an excess of protons and neutrons prefer to decay by emitting the α particle rather than other positively charged ones on account of the Q-value of α decay, Q_{α}, being positive and significantly high. This is because the doubly magic $^{4}_{2}He$ nucleus is a small, very tightly bound structure with a high binding energy per nucleon [9]. In two-particle decay kinematics, the particle energies are discrete for energy and momentum conservation. The kinetic energy of the α particle, K_{α}, can be expressed in relation with the daughter nucleus mass m_{Y}, α-particle mass m_{α}, and Q_{α} as follows:

$$K_{\alpha} = \frac{Q_{\alpha}}{1 + \frac{m_{\alpha}}{m_{Y}}}. \tag{2}$$

The mass of the α particle is significantly small compared to the daughter nucleus and, in effect, results in a small mass ratio which can be used to simplify the above relation to [10]:

$$K_{\alpha} = Q_{\alpha}\left(1 - \frac{4}{A}\right). \tag{3}$$

Gamow's Theory of α Decay and Geiger-Nuttall Law

A compelling description of the α-emission process is given by Gamow's theory of α-decay [11]. In this quantum mechanical description, the α particle is considered to be already pre-formed inside the nucleus even before the parent nucleus has undergone the decay. The α particle, with a kinetic energy of $Q_{\alpha} - V(r)$ at position r (Fig. 3), is held in a potential representative of the daughter nucleus and at times impinges on the potential barrier during its motion. The potential barrier is the region where the total binding potential is higher than the total available energy Q_{α}, in the α particle's disposal, rendering it unable to escape directly.

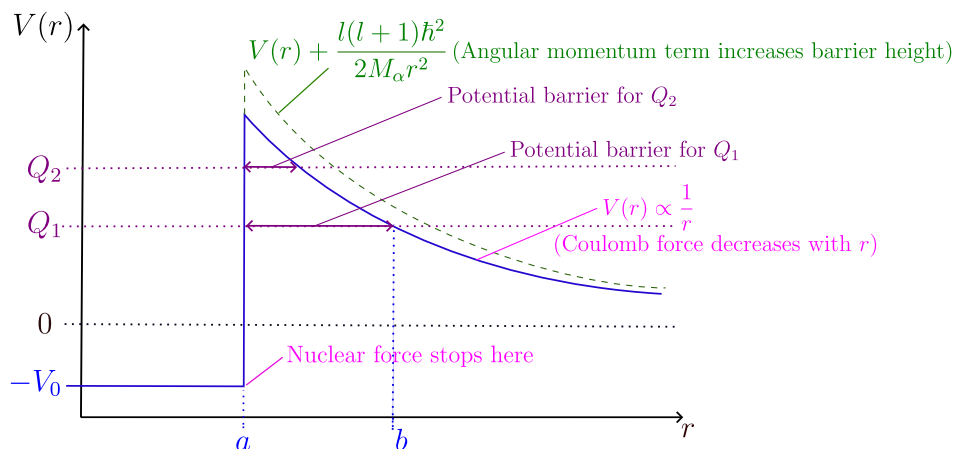**Figure 3:** Illustration of the relative potential energies in the α particle, daughter nucleus system using a simplified square well potential showing the potential barriers that need to be tunnelled through for two different Q_{α} values. The effect of the angular momentum term that increases the potential barrier is also shown.

6

Each time the α particle encounters the potential barrier, it has a certain probability to tunnel through the barrier, out of the parent nucleus and be emitted. The decay probability per unit time, λ – also called the decay constant – is then related to the frequency f of the α particle encountering the barrier and the probability P of tunnelling through it [11]:

$$\lambda = fP. \tag{4}$$

Due to the decay shape of the potential barrier – a result of the decreasing Coulomb potential with distance and short-range nuclear force potential that does not extend past the nucleus radius – a higher Q_α corresponds to a narrower barrier. A narrower barrier means a higher tunnelling probability and, in turn, an increased likelihood of α emission. The height of the barrier, i.e. the magnitude of the potential, is also important since a stronger potential is more difficult to tunnel through, having a low P. The value of P can be expressed in terms of a so-called Gamow factor G as $P = e^{-2G}$. G is dependent on m_α, Q_α, as well as the width and the height of the potential barrier.

The energy released in α decay has long since been found to be intertwined with the parent nucleus' observed half-life $t_{\frac{1}{2}}$. Those α emitters that decay faster have high Q_α values. The Geiger-Nuttall law, named after the first observers of the trend, states that there is an inverse relationship between the logarithm of the half-life and the square root of the decay energy Q_α [12]. The modern form of the Geiger-Nuttall law, with coefficients a and b that depend on Z and A, is in the form [13]:

$$\log t_{\frac{1}{2}} = \frac{b}{\sqrt{Q_\alpha}} + a. \tag{5}$$

This means for exotic nuclei, such as the neutron-deficient uranium region covered in this thesis work, which are expected to have rather large Q_α values of around $8\,\text{MeV}$ or more, the timescales in which the α emissions are expected to occur are quite short, falling in the microsecond or even in the nanosecond range.
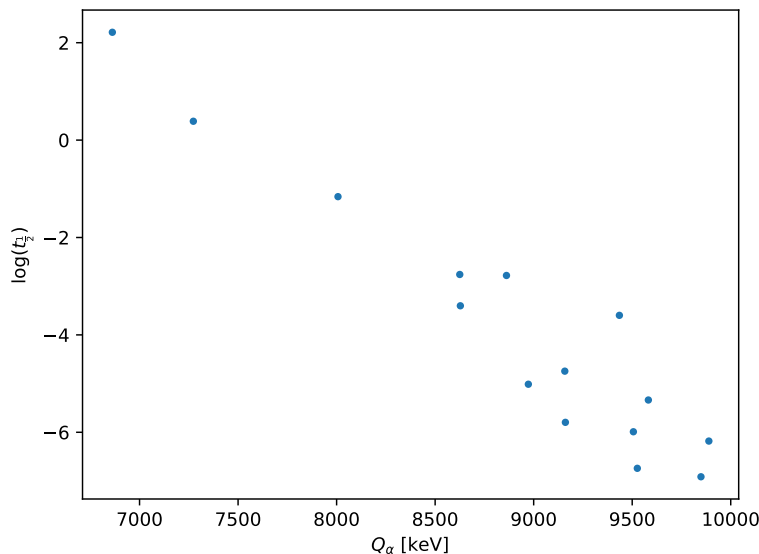

Figure 4: Geiger-Nuttall plot for nuclei in ^{221}U- ^{225}U decay chains using tabulated values [2].

7

Figure 4 shows how the Geiger-Nuttall plot looks in the region involving ^{225}U to ^{221}U decay chains. By the increase in Q_α from 7 to 9 MeV, the half-life changes from minutes to nanosecond timescales. Without the advent of fast sampling digitisers that allow the recording of digital pulse traces with sampling in nanosecond intervals and analyzing the pulses directly, catching these fast α particles emitted immediately after the formation of the exotic nuclei would be impossible. This resulted in the nuclear structure of many exotic nuclei being inaccessible for many decades after their discoveries until the technologies advanced in recent times [14].

Following the Geiger-Nuttall law, one is able to calculate $t_{\frac{1}{2}}$ from the Q_α value. However, it is often the case that the experimentally measured $t_{\frac{1}{2}}$ are longer than the calculated ones. Considering Gamow's theory of α-tunnelling, the Q_α dependence on $t_{\frac{1}{2}}$ have been found to be predicted correctly [15]. Hence, this inconsistency is likely a cause of effects besides tunnelling. In the tunnelling model, the decay constant λ is related to the frequency of α encountering the barrier and the tunnelling probability. λ is also the inverse of the mean lifetime of decay τ, which in turn is related to the half-life through $t_{\frac{1}{2}} = \tau \ln 2$. One can compare the calculated decay constant λ_{calc} derived using the calculated lifetime τ_{calc} from Q_α with the experimental decay constant λ_{exp} derived using the experimentally measured lifetime τ_{exp}:

$$\lambda_{calc} = \frac{1}{\tau_{calc}} \quad \& \quad \lambda_{exp} = \frac{1}{\tau_{exp}}. \tag{6}$$

The ratio of these two decay constants gives the hindrance factor h [15]:

$$h = \frac{\lambda_{exp}}{\lambda_{calc}} = \frac{\tau_{calc}}{\tau_{exp}} = \frac{1}{fP\tau_{exp}}. \tag{7}$$

The corrected decay constant for α decay, λ_α, then includes this hindrance factor:

$$\lambda_\alpha = hfP. \tag{8}$$

The value of h can lie between 0.1 to 10^{-6}. The magnitude of h indicates the significance of other effects besides tunnelling. These other factors that can affect α decay include – but are not limited to – the pre-formation factor of the α particle before emission, conservation laws – such as those for mass-energy, momentum, quantum selection rules –, the presence of unpaired nucleons, differences in the nuclear structure of the parent and daughter states, or nuclear shell effects.

Fine Structure of α Decay

In α decay, the parent nucleus transforms into a more stable, daughter nucleus by emitting an α particle. The daughter nucleus that results from the decay is not always in the ground state with the lowest energy but rather can populate different states depending on nuclear structure constraints and selection rules. This gives rise to different decay paths of similar energies. This is what we call the α-decay fine structure. The α-energy line splits into 'branches' where each branch goes into a different daughter nuclear state. Branching ratios are assigned to indicate which α-decay paths are more likely. Generally, this is the transition

when going from a ground state, parent nucleus into a ground state, daughter nucleus. The decay scheme in the ^{225}U decay chain including the known α-decay fine structure is displayed in Fig. 5.
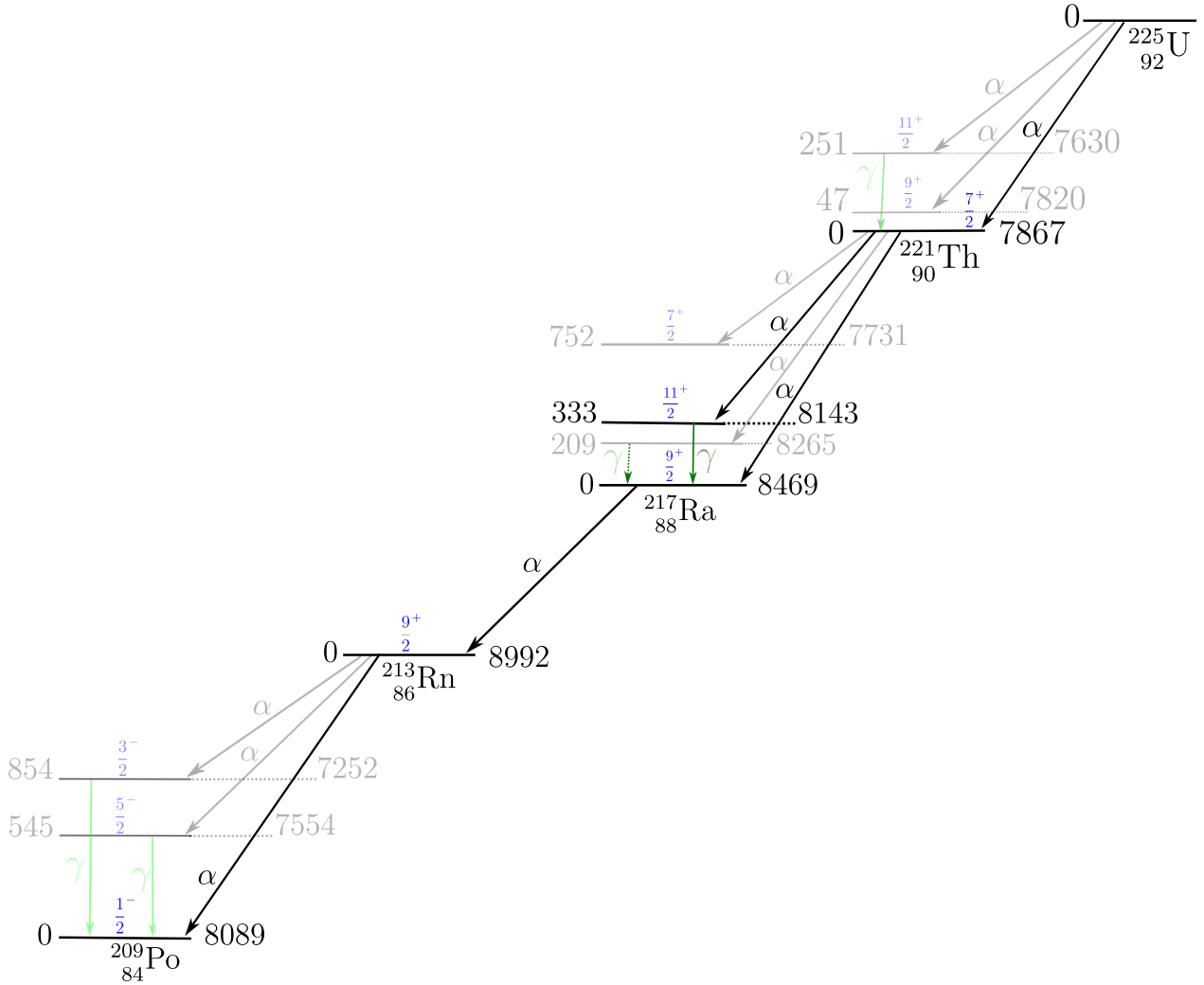

Figure 5: The decay scheme for the $^{225}_{92}$U isotope. Decay modes that are suppressed are decreased in opacity to highlight the decay path that is expected to be observed most frequently during experiments. The α-particle kinetic energies are given to the right of the levels, the energy levels relative to the ground state are given on the left, and known spin-parity values are given on top in blue. Observed γ transitions are also shown. The data used are from NNDC nuclear datasheets [2].

The transition in nuclear states is controlled by selection rules based on conservation laws where angular momentum and parity conservation are the most important. The angular momentum of the α particle, when emitted from a parent nuclear state of angular momentum I_P resulting in a daughter nuclear state of angular momentum I_D, can take values between $|I_P \pm I_D|$. The α particle has spin 0 – a consequence of the pairing of two protons and two neutrons in their ground states. The total angular momentum of the α particle, thus, only arises from its orbital angular momentum l_α. Additionally, the parity change brought about by the α particle is $(-1)^{l_\alpha}$ and to conserve parity, the relation $\pi(I_D)(-1)^{(l_\alpha)} = \pi(I_P)$ has to

be satisfied. This means for transitions between nuclear states of the same parity, l_α is even, while l_α is odd when the nuclear states have opposite parity [16].

The angular momentum adds a layer of centrifugal barrier to the potential barrier that the α particle tunnels through (see Fig. 3) and the tunnelling probability becomes smaller. Transitions to excited states have lower Q_α values which means a thicker potential barrier has to be tunnelled. Again, this results in a decrease in the probability of that particular α-decay path. Both higher l_α and lower Q_α suppress the α decay and lower the branching ratio, but the effect of lowering Q_α is far more significant. This corresponds well with the Geiger-Nuttall law covered in the previous sub-section.

Additionally, similar nuclear structures in the parent and daughter nuclei are preferred. For most even-even nuclei, the ground state, 0^+, to ground state, 0^+, transitions are the most dominant decay branch and they have the highest Q_α. Here, the nuclear structure of the states before and after the transition are comparable. On the other hand, odd nuclei have an unpaired nucleon that results in an overall spin and is sometimes responsible for the nuclear structural properties (based on the extreme single-particle shell model). The parent and daughter ground states can also have very different nuclear structures due to different unpaired nucleons present. However, some excited states of the daughter nuclei could have a similar nuclear structure to the parent nuclei, resulting in those decay paths being favoured. An example of this is seen in the branching ratios in the odd ^{221}Th fine structure in Fig. 5, where the second excited state is the most preferred branch. Nuclear deformation, a feature present vastly in heavy nuclei, also affects the α-decay process. The shape of the deformed nuclei brings about differences in the potential barrier from the poles to the equator and also determines the angular momentum distribution of the α particles being emitted from different points. Thus, these nuclei will have a preference for decay paths depending on whether the α particle is being emitted from the poles or the equator [17].

The daughter nucleus when populated in an excited state can undergo further α decay – or other allowed decays – from the excited state if it is radioactive. However, excited nuclei generally first undergo nuclear relaxation into lower energy states up to the ground state in one or more transitions. There are two main types of nuclear relaxation, namely γ decay and internal conversion (IC). The dominant process is the γ-decay process, where the excited nucleus de-excites by releasing energy equivalent to the difference in energy levels in the form of a γ photon. These photons are emitted, with half-lives normally in the order of picoseconds, following the α emission, i.e. the photons come in rapid coincidence. These coincidences are also called 'prompt'. The second nuclear relaxation process that occurs depending on nuclear and atomic structure is internal conversion where the energy to de-excite is released by the emission of an atomic shell electron manifested through electromagnetic interaction between the nucleus and the orbiting electron. Since, this creates holes in the inner atomic shell, X-ray photons or Auger electrons or both follow [18].

Since the nuclear states have fixed energies that are unique, combining the α-decay energy with the γ-decay energy or the energy of the conversion e^- that may come in prompt coincidence, and comparing the total with other α-decay energies allows one to check if

the α-decay energies seen are part of branches diverging from the same parent nuclei. This can be seen in the α-decay fine structures in Fig. 5 where an energy state in the daughter nucleus is reached directly through one α-decay transition or in steps consisting of an α-decay followed by a γ-decay transition. This has important uses in α-photon spectroscopy – the experimental technique related to this thesis work – that will be introduced briefly in the coming sub-section and allows to discovery of new nuclear states or verify known ones through α-decay fine structure determination.

2.3   Introduction to α-Photon Spectroscopy

α Decay can provide an enormous amount of nuclear structure information, allowing one to determine nuclear states from the decay energies and fine structure, while also better understanding inconsistencies in nuclear structure trends due to shell effects. With technological advancements, studies of exotic nuclei – with very short lives in the microseconds range or lower and lying in the heavier region of the nuclidic chart where α decays are prominent – have become an exciting and resourceful domain for α-photon spectroscopy. The exotic nuclei in the desired region are synthesised in the laboratory typically bombarding a high-energy beam of one nuclei type into a target of a second type, that would synthesise into a third nuclei type. Specific reaction channels are selected by tuning the beam energy that would yield the highest cross-section of the formation of desired ones while suppressing others. The synthesised nuclei must be separated within their lifetimes and transferred into a decay station specialised for charged particle and photon detection.

The particle detectors that give the best energy resolution at present are doped semi-conductor detectors that work by creation of electron-hole pairs acting as charge carriers on interaction with ionising radiation and registering current pulses that are then converted into voltage pulses, proportional to the ionising particle energy, using preamplifiers [19]. Fast sampling electronics are also necessary to be able to record and distinguish energy depositions in small time intervals of microseconds or lower. The retrieved energies and intensities of charged particles and photons are analysed. Alpha particles are characterised by energies from around $5\,\mathrm{MeV}$ to $11\,\mathrm{MeV}$, with the ones emitted from more exotic nuclei being in the higher energy region. A sequence of correlated α decays observed are decay chains. Using the combined results, the overall decay scheme can be determined. Measuring the time between energy depositions and being able to tag correlating ones allows one to determine the half-lives of the decaying nuclei, and calculate hindrance factors and branching ratios. Self-consistent comparisons of the decay paths from experiments with simulations can aid in establishing the nuclear structure properties of the observed states. All this valuable information is what was aimed to be extracted during this thesis work from analysing data on the exotic nuclei, in the neutron-deficient uranium region, recorded in the α-photon spectroscopy measurements performed during the U310 experiment. The part of the experiment relevant to this degree project, the corresponding data analysis, the latest results, and the outlook for further research in similar areas are covered in the following sections.

3   The U310 Experiment

The U310 experiment took place at the `TASCA` beamline of the GSI Helmholtz Centre for Heavy Ion Research, located in Darmstadt, Germany. It was carried out over two runs, one in 2019 and the other in 2020, for spectroscopic studies along the decay chains of the superheavy element $Z = 114$, flerovium.

At the beginning of each of those experimental runs, reactions of accelerated ^{48}Ca / ^{50}Ti ions with a hafnium target were used to help investigate the response of consecutive energy depositions occurring within a very small time interval – such that they are recorded in the same digital trace of the preamplifier – in the same pixel of the central implantation detector (described in later subsections). These so-called pile-up signals were recorded to have data to develop a dedicated analysis routine for their analysis which was necessary for the main experiment, while at the same time allowing further work such as the one covered in this thesis to be carried out. The pile-up analysis routine would allow for retrieval of the energies and timings of fast α-emissions ensuring accurate decay chain determination when fast α-decaying nuclei are present.

In this section, the details of the experimental setup are given with a focus on the part of the experiment where $^{nat.}$Hf was used as a target. The decay station `TASISpec+`, which is an improved version of `TASISpec` [20], is described along with the functionality and features of the different components. In the final part of the section, the data acquisition system that handles the processing of raw energy signals into analysable digital ones is covered.
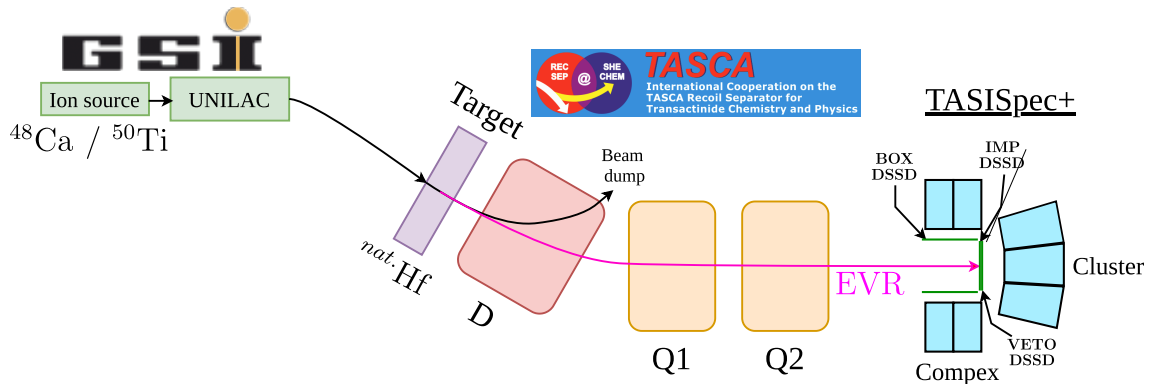
3.1   The Experimental Setup

Figure 6: A schematic diagram of the experimental setup showing the different components involved from the delivery of beam ions on the target wheel to the impingement of the EVR in the decay station. The figure was modified from Ref. [1].

A schematic representation of the experimental setup is shown in Fig. 6. The GSI Universal Linear Accelerator (`UNILAC`) delivered ions of ^{48}Ca^{10+} and ^{50}Ti^{12+} in a pulsed beam structure having the beam on for 5 ms followed by the beam off for 15 ms. The ^{48}Ca and ^{50}Ti ion beams at 4.72 MeV/u and 4.75 MeV/u, respectively, were guided to the `TASCA` experimental hall

where the target station is situated. The ions impinged a rotating target wheel of natural hafnium electroplated onto a backing support made of $2.1\,\mu m$ thick titanium foil, where the backing faced the direct beam. The target wheel rotates synchronously with the pulsed beam structure enabling a high and even beam intensity across the entirety of the target surface.

Due to a long-standing issue with the energy modulation at `UNILAC`, the energy of the ion beam was attenuated to desired values using sets of titanium foils as a means to select specific channels for fusion-evaporation reactions. In these reactions, the resulting compound nuclei have low excitation energy and usually release two to five neutrons when forming fusion-evaporation residues. The evaporation residues (EVRs) that recoil out of the target were carried with the beam into the gas-filled separator `TASCA` – TransActinide Separator and Chemistry Apparatus [21]. `TASCA` was filled with $0.8\,mbar$ of He gas to provide an average charge that allowed to filter out the fusion-evaporation products – based on the A and Z values – from the rest of the beam-like and target-like non-fusion reaction products with its dipole magnetic field. The separation occurred based on the different mass-to-charge ratios of the particles in the beam cocktail which was proportional to the $\frac{A}{Z^{1/3}}$ ratio since the charge of the particles gets evenly distributed within `TASCA`. The EVRs were next directed into the decay station '`TASISpec+`', an upgraded version of `TASISpec` (`TASCA` in Small Image mode Spectroscopy) [20], through focusing facilitated by two quadrupole magnets. The decay station is described in the next section detailing all the components and features that enabled high-resolution α-photon-electron spectroscopy of the implanted EVR.

3.2 TASISpec+

`TASISpec+` is a configuration of a cube of silicon detectors which are, in turn, surrounded by germanium detectors. It is a decay station with enhancements performed on its predecessor `TASISpec` and will be succeeded by the `LUNDIUM` decay station in the future [14]. A rendered model of `TASISpec+` is presented in Fig. 7(a).

(a) Model of the `TASISpec+` decay station   **(b)** The Si cube.
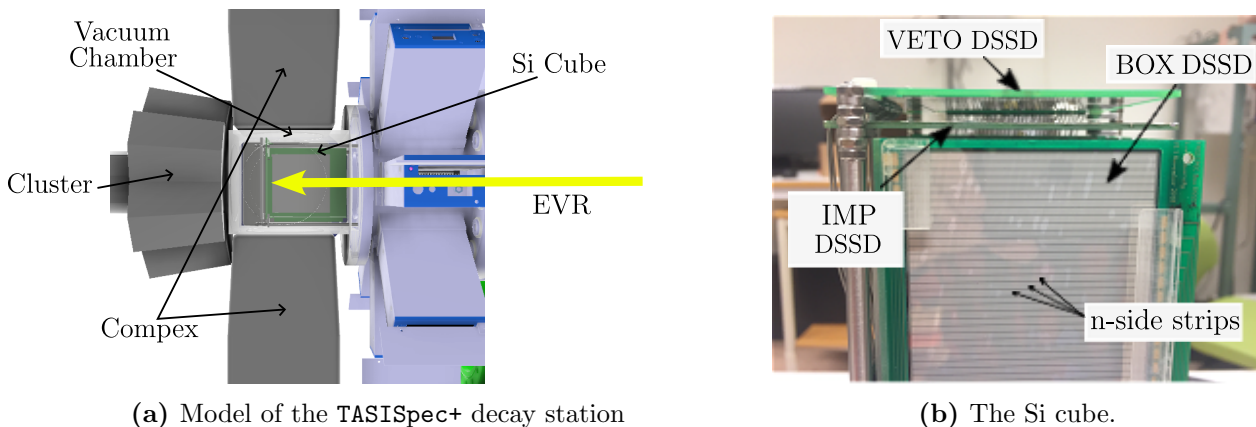
Figure 7: A 3D model of the `TASISpec+` decay station with all its components and a close-up image of the Si cube that shows the different components and the n-strips on the outer face of the visible BOX detector. Both figures are adapted from Ref. [1].

The central part consists of an open 'Si cube' dedicated to charged particle detection. This

Si cube consists of six pixelated Si detectors placed in a box-like configuration with one side left open to let the EVRs in. The exterior walls are made of aluminium (0.5-1.0 mm thick) and the side left open is connected to the separator, i.e., `TASCA`. The EVRs implant on a 0.31 mm thick, 32×32-strip double-sided silicon-strip detector DSSD referred to as the implantation detector or IMP DSSD. This is the primary detector where the recoil energies of the implanted nucleus and the α particles are registered. Additionally, four 0.97 mm thick, 16×16-strip DSSDs are positioned upstream on the four edges of the IMP DSSD forming an open box layout. The purpose of these so-called BOX DSSDs is to try to capture backward-recoiled α-particles that escape the IMP DSSD with only partial energy deposition. By combining energy depositions in the BOX DSSDs that come in coincidence with energy depositions in the IMP DSSD, it is possible to reconstruct the 'full' energies of those backwards-recoil α particles that would have been otherwise missed. As a result, this increases the efficiency of reading out all the α particles from the α-decaying implanted nuclei and allows one to determine their complete decay chains more precisely. There is still about 20 % chance of the α particle to completely escape if it recoils back upstream in the beam axis where there are no detectors but the overall escape rate is significantly reduced [1].

The last part of the Si cube and one of the new additions in the `TASISpec+` setup is the installation of a veto detector. The veto detector, dubbed VETO DSSD, is a second DSSD identical to the IMP DSSD situated directly behind it. Due to mechanical constraints of `TASISpec`, it had to be rotated by an angle of 90° and slightly shifted in position with respect to the IMP DSSD [22]. Checking for energy signals in both the IMP DSSD and VETO DSSD enables one to differentiate between energy events of different radiation types – such as high-energy β radiation from low-energy depositions by escaped α-particles. Overall, the selection of interesting events – from the typically, many millions of events – is enhanced which ensures that a cleaner final spectrum is achieved. Further details of the VETO DSSD and its importance can be found in Ref. [19].

An image of the Si cube with visible strips on the BOX DSSD is shown in Fig. 7(b). The DSSDs have strips on both front and back sides where the front, i.e. the inner face, is referred to as the p-side while the back is referred to as the n-side. The p-side strips are arranged perpendicular to the n-side strips such that their intersection forms a virtual lattice of pixels. The pixelation allows two-dimensional tracking of implanted nuclei and their decay. Effectively, it increases the number of implants that can be measured distinctly at any one time. Additional details of the DSSDs and their working principles are available in Refs. [19, 23].

Ge detectors are positioned around the Si cube for photon detection. Four novel Compex germanium detectors [24], each having four cubic Ge crystals, are placed behind each of the four BOX DSSDs. This is the most prominent upgrade included in `TASISpec+` which significantly improved the efficiency of low-energy photon detection. Lastly, the usual seven-crystal Cluster Germanium detector is situated behind the IMP-VETO DSSD back-to-back setup [1]. The total five composite Ge detectors played the crucial role of highly efficient photon detection that may follow alpha decays to excited daughter states as well as the low energy X rays following internal conversion.

All of the DSSDs were connected to preamplifiers, while the germanium detectors have built-in preamplifiers. The preamplifiers were read out with fast readout digitisers to process the energy signals created by ionising radiation. The next sub-section discusses the processing of these energy signals and the data acquisition system used.

3.3   Processing of Energy Signals and the Data Acquisition System

Figure 8 visualises the flow of data from the decay station to being ready for analysis. The $(2 \times (32+32) + 4 \times (16+16)=)$ 256 channels from the DSSDs were cabled to eight 32-channel, Cologne-produced, charge-sensitive preamplifiers to collect the current pulses, i.e. ultimately energy signals, generated from the energy deposition by the decay products. The preamplified signals were read out utilising GSI-developed, fast digitiser cards, `FEBEX` [25]. The `FEBEX` cards, version 3B, are 14-bit sampling analog to digital converters (ADCs) operating at 50 MHz. They have FPGAs from which the energy and time of the preamplifier signals were recorded [1].
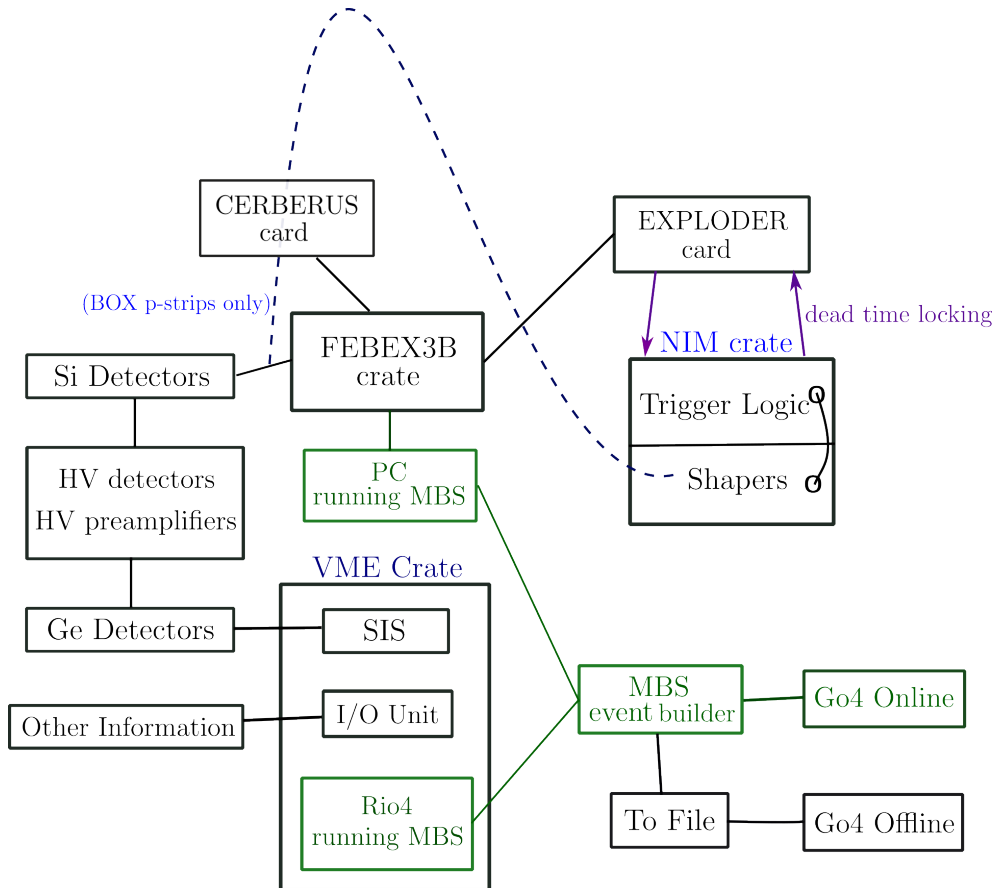

Figure 8: The schematics of the data acquisition system which show the connections between the different components. The `EXPLODER` card – which takes care of accepting trigger signals depending on whether a preamplifier trace is already being recorded or not – is also included.

The $(4 \times 4 + 7=)$ 23 channels from the five Ge detectors were read out with five commercial

`VME SIS3302` 16-bit sampling ADCs operating at 100 MHz [26]. The flat-top energy, baseline, time, and pile-up recognition flag in the preamplified Ge signals were recorded from them. The GSI Multi-Branch System (MBS) data acquisition software [27] is used to acquire the data from the `FEBEX3B` cards and `VME SIS` modules which have been processed into list-mode data – a computer-readable and storable format. It reads out both `FEBEX3B` and `VME` branches and builds a combined event. Energy signals that satisfy set thresholds were used as trigger requests to initiate the recording of data. In this preparation part of the U310 experiment, the triggers were tuned to obtain the best settings for the main experiment. In the final version, the two initial triggers used were an energy signal of 150 keV or more in the IMP DSSD, or an energy signal of about 5 MeV or higher in any of the BOX DSSDs. The latter ensures that any α particle that escapes from the IMP DSSD – depositing very little energy there – into one of the box DSSDs still triggers. Once one of these initial event triggers was set off, all subsequent signals above 150 keV were recorded. For the Si DSSDs, `FEBEX3B` traces of 80 µs length, and for the Ge detectors, `SIS` events of 5 µs were recorded. Since there were different thresholds for the triggers but the `FEBEX3B` cards only supported a single trigger threshold, an innovative extra readout layer had to be implemented. The p-strip channels of the BOX DSSDs were replicated with `CERBERUS` cards. This allowed one output of the channels into the standard `FEBEX3B` cards, while the other replicated output into a mesytec `MSCF` [28] shaping amplifier that would be responsible for generating the corresponding trigger signal. An `EXPLODER` card is connected to the `FEBEX3B` cards to handle dead-time locking i.e. accepting trigger signals depending on whether a preamplifier trace is already being recorded or not. An input/output (IO) register module was used to write general event information into the data stream. These included beam status (off or on), target segment, trigger type, and chopper state (in or out) [1].

A beam shutoff routine was implemented in the data acquisition system such that a triggered event signal initiated an electrostatic chopper into the beam near the ion source during beam-on periods to cut off the beam completely for a programmable length of about 200-300 s [1]. This prevents additional implantation events that otherwise interfere with an ongoing decay chain that would make it impossible to determine which implanted nuclei the α particles are being emitted from. During the main experiment, this beam shutoff routine was used. However, during the preparation stage using the $^{\text{nat.}}$Hf target, the response of the silicon detectors to fast pile-up signals was being investigated in order to improve the algorithm for handling pile-up signals for the main experiment, and the beam shutoff routine was not used. Moreover, most of the expected α particles from the decay chains in the produced implanted nuclei region have very short half-lives – guaranteeing the production of pile-up signals – with many chains ending within nanoseconds. This means that the beam shutoff routine would very much be impractical and might not even have enough time to remove the beam completely by the time the decay chain had been completed. This means a lot of valuable beam time could be lost. To obtain the energies of subsequent, fast α particles appearing as pile-up signals in a single `FEBEX3B` trace, a dedicated analysis routine has to be performed on the digitalised preamplifier traces. This trace analysis routine for handling pile-up signals, vital to this thesis work where α particles mostly come as pile-ups, is described in the following subsection.

3.4 Trace Analysis of Pile-up Signals

The energy of the signals for single pulse traces can be retrieved as FPGA values directly from the FEBEX digitiser. A sketch of this energy retrieval procedure is shown in Fig. 9. FEBEX performs an m-step differentiation where it takes differences between sample values – where a sample is one single point in the digitised trace – over m-steps that results in a near trapezoid shape since the pulse rises sharply at the trigger time and falls in an exponential decay. Taking the average around the top of this trapezoid gives the energy. The energy retrieved from this simple trapezoidal filter method is already very accurate but it is still further improved using a moving window deconvolution MWD algorithm [29].
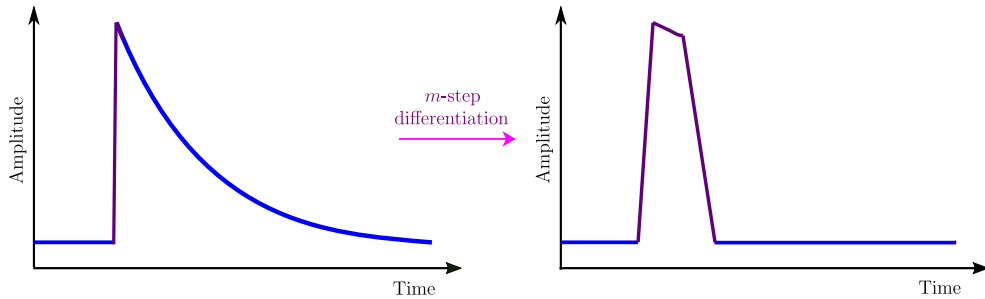

Figure 9: The transformation stages of the energy pulse when transformed using a trapezoidal filter by the FEBEX digitisers to obtain FPGA energies.

The MWD procedure consists of three primary steps: a deconvolution, an m-step differentiation, and a moving average. The MWD process applied to a single pulse trace is illustrated in Fig. 10.
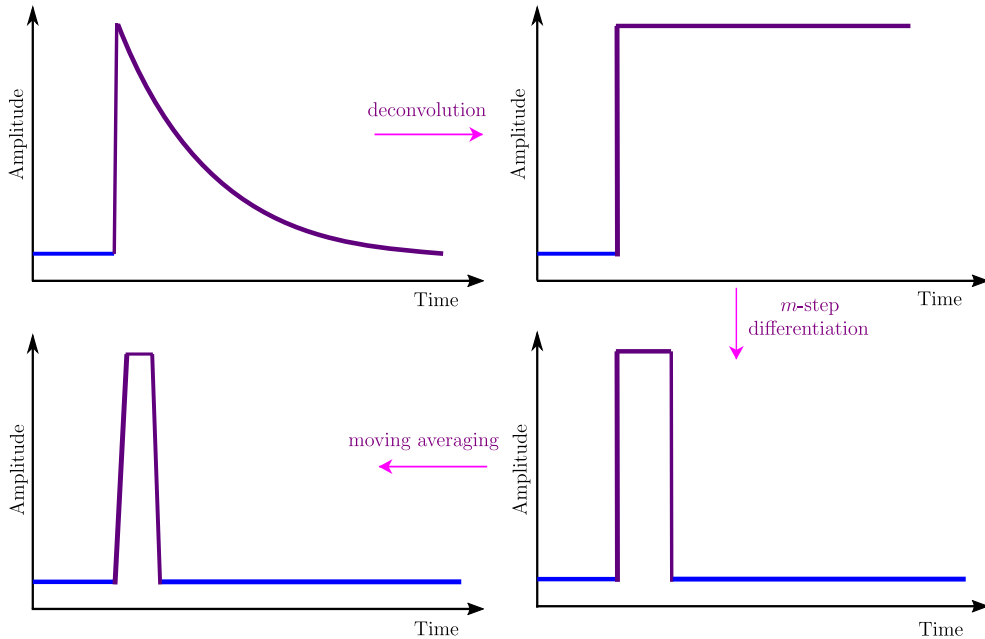

Figure 10: The moving window deconvolution when applied to a preamplifier trace with a single pulse. The arrows indicate the signal processing steps. Step 1 is the deconvolution, step 2 is the m-step differentiation, and step 3 is the moving averaging.

The preamplifier signal is basically an output produced from the convolution of the energy deposition, which can be described by a step function with full energy at the step, and a transfer function dependent on the properties of the DSSD strip and preamplifier mechanics. The transfer function is known and can be used to find out the input signal, i.e. the energy deposition, through a deconvolution. The deconvolution forms a step-like pulse at the point of energy deposition with an average height at the step proportional to the energy. A m-step differentiation is further performed on the deconvoluted signal which transforms it into a box-shaped signal. Finally, taking moving averages within a narrow sample interval along the box-shaped pulse produces a trapezoidal pulse from which the energy is retrieved as the average at the flat top.

`FEBEX3B` firmware was not set to retrieve the energies from the subsequent pulses in traces containing pile-up. It provides the first energy and flags the trace as containing pile-up. Recording the traces to disk and using a pile-up analysis routine is then required to run to obtain the energy of every pulse appearing as pile-ups. The procedure is similar to the usual deconvolution method but baseline correction needs to be performed on the subsequent pulses which are technically 'riding' on a preceding, deconvolved pulse. This is taken care of directly by the m-step differentiation. The MWD process applied to a pile-up trace is displayed in Fig. 11.
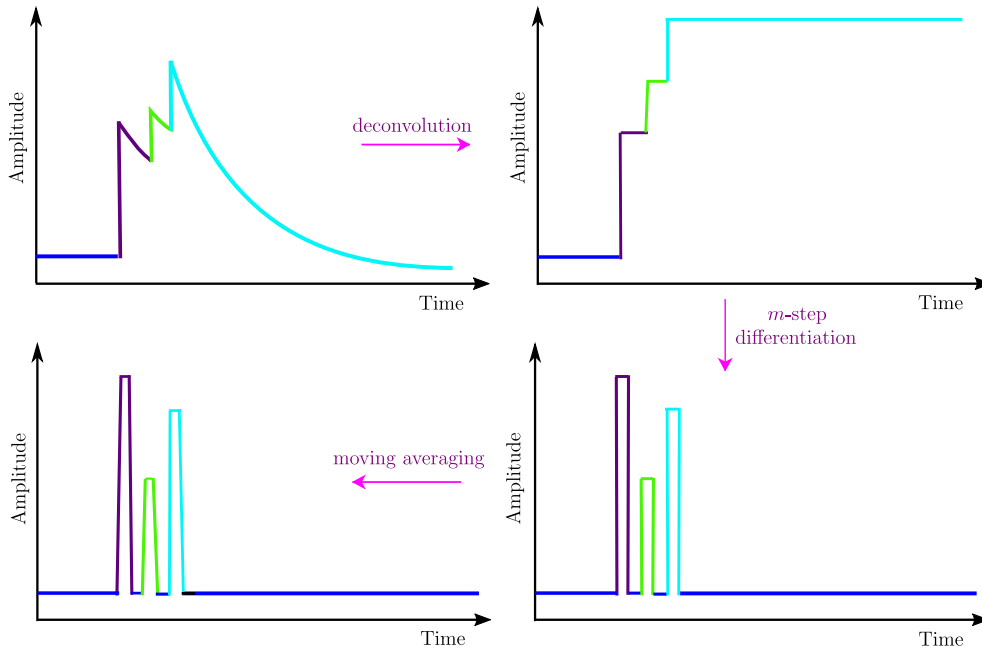

Figure 11: The moving window deconvolution when applied to a preamplifier trace having pile-up. The arrows indicate the signal processing steps. Step 1 is the deconvolution, step 2 is the m-step differentiation, and step 3 is the moving averaging. After step 1, the shifted baseline following deconvolution is visible.

First, the deconvolution step transforms the trace pulses into a climbing step function, where each new step has the combined energy of all pulses in the trace up to the pulse occurring at that step time. The baseline is thus shifted but the difference between the steps would

still give the energies. To determine the energies more accurately, an m-step differentiation is performed which forms box pulses and removes the baseline. Moving averages within a narrow sample interval are taken along the box pulses to form trapezoidal pulses where the averages at the flat tops give the energy of the pulses. The moving averaging is very important in both the single pulse trace and the pile-up trace. This is because the actual signal is noisy – unlike the smooth signals shown in the illustrations used here to help follow the signal processing – and just taking a single energy point at the plateaus after the deconvolution or m-step differentiation does not give the most accurate energy value.

The analysis of digitised preamplifier traces using the moving window deconvolution routine is just one part of the entire data analysis procedure. This is a time-consuming procedure because the traces contain an enormous amount of data samples that are processed to retrieve the energy and time of events while also handling pile-up signals. Hence, this is done in the early stages separate from the rest of the data analysis – specifically in the unpacking step of the Go4 analysis framework that will be described in the coming section – to speed up the main analysis. The complete data analysis that was carried out starting from processing the saved List-Mode Data files to the determination of identified decay chains is covered in the next section. Additionally, important energy corrections that were performed as well as the process of selecting prompt α-photon coincidence are emphasised.

4   Data Analysis

The raw data from the silicon preamplifiers processed by the `FEBEX3B` digitisers and the built-in germanium detector preamplifiers processed by `VME SIS3302` modules, along with other statuses recorded by the input-output module, are stored as List-Mode Data LMD files. This stored data requires preparation before it can be efficiently used. For that purpose, the GSI-developed Go4 analysis framework was utilised in major portions of the data analysis [30]. The flow chart of the Go4 data analysis procedure implemented is presented in Fig. 12.
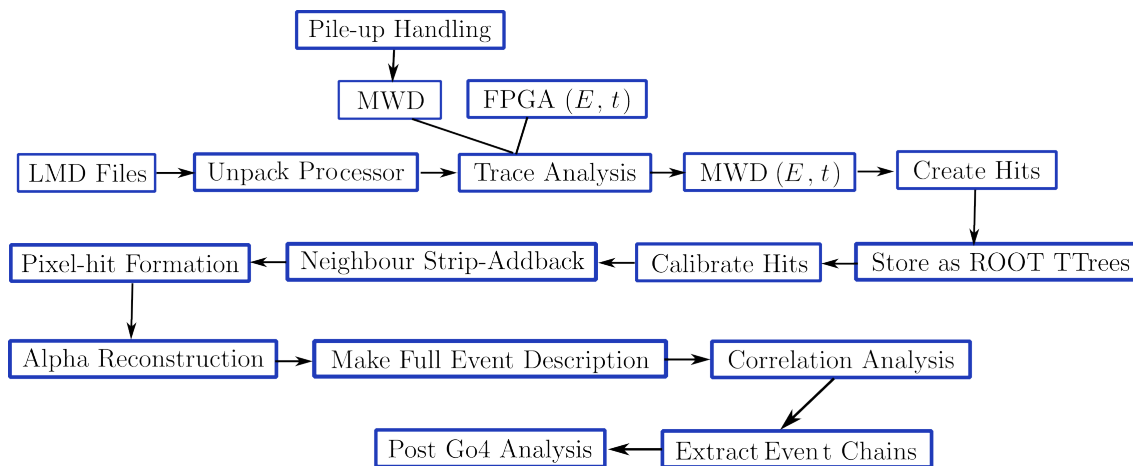

Figure 12: The flowchart of the data analysis carried out in Go4 preparing the data to be used in the post-Go4 analysis.

The Go4 framework works by dividing the analysis procedure into steps. Each step primarily consists of a pre-event, a processor, and a post-event part. The pre-event data are processed by the processor into post-event data. The post-event could be further followed by some post-event analysis or processing step. The main processes in the data analysis carried out in Go4 for the experiment covered in this thesis included unpacking the LMD files, calibration of the detector channels, pixel formation using the calibrated channels, α-energy reconstruction for coincident hits in IMP and BOX DSSDs, matching IMP DSSD events to coincident photons in the Ge detectors, and finally using the processed full event description to build chains of correlated α decays.

The first step – the unpacking step – takes the binary, LMD files and converts them into more meaningful C++ ROOT TTree files which are easier to be prepared for analysis. The main part of this step is the application of the aforementioned trace analysis routines involving the moving window deconvolution applied to the digitised preamplifier traces of the silicon detectors. This retrieves the most important information which is the energy and the time of the energy pulses, including pile-ups. The traces contain a large number of data points, i.e. samples, which take large amounts of memory and require a comparably long time to be analysed, making it not preferable to be carried out every time during the main chain hunt analysis. The unpacking process needs only to be carried out once and when the 'unpacked' event with the energy and time of all signals is available, the rest of the trace can be discarded speeding up further analysis. Next, from the energy and time, detector channel hits are created. The channel hits correspond to a unique detector ID with uncalibrated energy and time relative to the event trigger. All these data are organised in ROOT TTrees. These 'unpacked' ROOT files also contain other important event information: beam status, chopper status, target segment, and event trigger type.

Next, the energies of the detector channel (strips for the DSSDs and crystals for the Ge) hits were calibrated. Though not part of this thesis work, the calibration data for the germanium detectors was obtained using a ^{152}Eu source, followed by routine recalibrations during the main experiment for in-beam energies using well-known gamma lines from (n, γ) reactions of ^{74}Ge and ^{28}Al along with the e^+e^- annihilation peak [1]. All the calibration energies for the germanium detectors considered in this work were taken from beam-off periods and at least $10\,\text{ms}$ past the beam pulse to ensure usability. For calibration of the DSSDs, a four-line α source with characteristics peaks around $5\,\text{MeV}$ from ^{148}Gd, ^{239}Pu, ^{241}Am, and ^{244}Cm was used. Further in-beam and implant calibrations were carried out during the main experiment. For in-beam calibration, energies of α particles from well-known nobelium isotopes, produced in reactions between Ca ions on a Pb target, were used [1].

Following the calibration of the strip hits, the 'pixel' hit formation was carried out. In some cases, two neighbour strips had hits at the same time and we assume that it was an 'inter-strip' event. The energies of these neighbour strip hits were added together to get the total energy. This total energy was assigned to the strip with the higher energy. Finally, coincident hits of similar energies in the p- and n-strips allowed the formation of pixel hits. It is also possible to carry out a similar add-back procedure for neighbouring Ge crystals but this was not highly significant for the low numbers of coincident photons observed.

Before the final part of the Go4 analysis procedure, coincident hits in the BOX DSSDs, VETO DSSD, and Ge detectors were all connected to each corresponding pixel hit in the IMP DSSD which sums up into full event descriptions. For coincident hits in the BOX DSSDs, full α energies were reconstructed where applicable. The full event data are then analysed in the final part of the implemented Go4 analysis procedure where chains of correlated α-decay events are built up. The algorithm used to hunt for the correlated α chains and the subsequent chain analysis performed to identify real α-decay chains are explained in the proceeding subsection.

4.1 Hunt for Correlated Event Chains

The main goal of this thesis work was to determine α-decay chains of the created isotopes in the actinide region of the periodic table. To achieve that, an algorithm to build up possible chains present in the recorded data was implemented. This last step in the Go4 analysis procedure, referred to as the correlation analysis, was at the heart of the chain hunt process. A chain in this context is a stack of correlated events recorded in the IMP DSSD as well as connected events seen in coincidence in the BOX DSSDs and Ge detectors. An illustration of the chain searched for in a pixel of the IMP DSSD is presented in Fig 13.
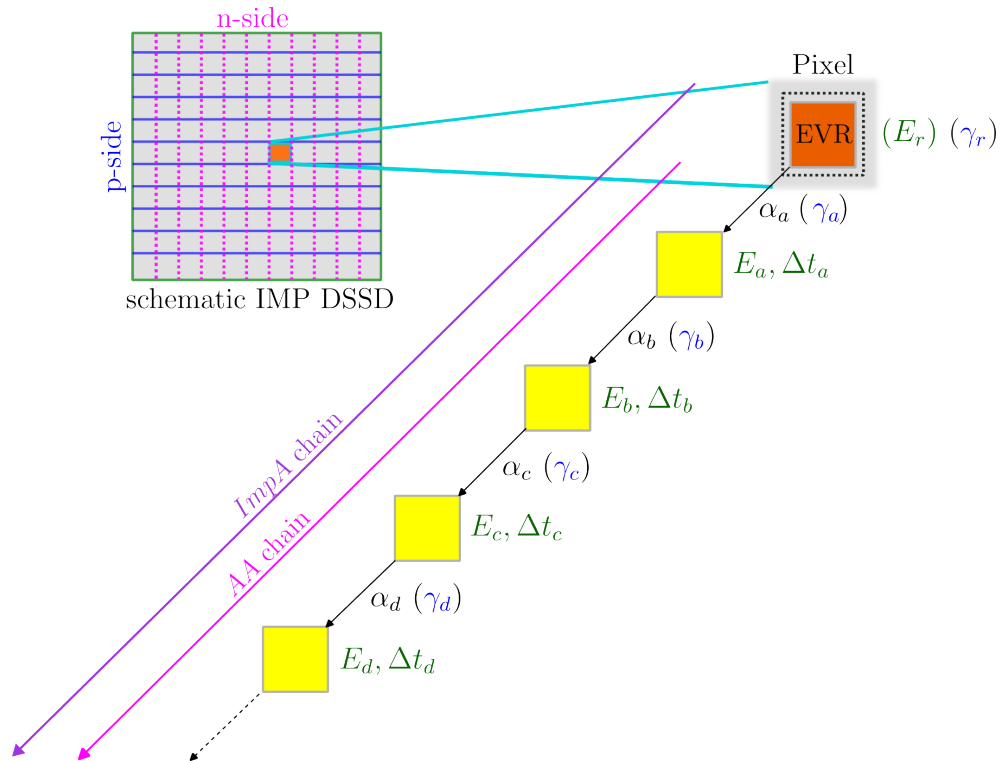

Figure 13: Illustration of the series of events extracted in the chain hunt algorithm of the Go4 correlation analysis. The two kinds of extracted chains indicated could be restarted at any point in the chain as explained in the text.

One follows the story of each pixel separately for all the IMP DSSD pixels. Chains found

in a pixel are stored as pixel-hit (ph) vectors. Two different kinds of chains are stored: one that starts with an EVR implantation event of energy E_r, and another that starts with an α particle (denoted α_a) with energy E_a. The size of the current pixel-hit vectors of both kinds are zero at the start, and the pixel-hits recorded for the pixel are checked for specified energies corresponding to an EVR implant or an α_a particle. The EVR implantation energy generally has much higher energy than those for α particles and is seen only during beam-on periods, while the α_a event could be seen in either beam-on or beam-off periods. When a ph satisfies the specified energy criteria, the ph – with all its related information – is pushed into the relevant ph vector: an $ImpA$ chain for an EVR implant, while an AA chain for an α_a. Now, that the sizes of the current chains are no longer zero, the proceeding ph is checked to see if it satisfies energies and event times, relative to the last pushed ph, corresponding to events further down the chains. For the $ImpA$ chain, the cross-checked event would be α_a with energy E_a within a relative event time of Δt_a. For the AA chain, the cross-checked event would be α_b with energy E_b within a relative event time of Δt_a. As before, if the ph satisfies the criteria for the searched event, it is pushed into the chain and skipped otherwise. Afterwards, the ph is further checked to see if its energy, but not time, again satisfies an α_a or an EVR implantation event. Every EVR implantation event restarts the $ImpA$ chain, while every α_a event restarts the AA chain. The entire process is repeated with successive ph where the event to be searched is updated with an increase in the size of the chains. Additionally, for all the ph that were pushed into chains, any photons in the Ge detector or potential electrons in the BOX DSSDs that came in prompt coincidence – covered in a later subsection – were also stored along with the ph. Finally, all of the chains of correlated events found are saved into a tab-separated values (tsv) file that has all the necessary information in a suitable format, ready for further analysis. At present, the algorithm can build chains until the last ph vector contains the event α_c which appears to be sufficient for the dataset analysed where most of the expected decay chains are expected to be limited to three α emissions, i.e. upto α_c. A chain of four α decays, $[\alpha_a\text{-}\alpha_b\text{-}\alpha_c\text{-}\alpha_d]$, could still be built replacing the energy criteria for the EVR implantation to that of α_a, but the event will only be searched during beam-on periods as if it were an implant. Details of how the described correlation analysis step was run repeatedly with various parameters, adjusted recursively, to build correlated event chains of interest and how the output chains were investigated to determine α-decay chains are given in the subsection that follows.

4.2   Post Go4 Analysis of Extracted Chains

The final part of the data analysis involved the use of the extracted chains of correlated events from the Go4 analysis to establish α-decay chains and build decay schemes. The key fusion-evaporation reactions between the beam nuclei (^{48}Ca / ^{50}Ti) and the natural hafnium target, which determined which region of the nuclidic chart was of interest, are as follows:

$$^{48}_{20}\text{Ca} + {}^{\text{nat.}}_{72}\text{Hf} \rightarrow {}^{A}_{92}\text{U} + 3n. \tag{9}$$

$$^{50}_{22}\text{Ti} + {}^{\text{nat.}}_{72}\text{Hf} \rightarrow {}^{A}_{94}\text{Pu} + 3n. \tag{10}$$

Only the $3n$ reaction channel is considered since it should have the higher cross-section based on the beam energy while the $2n$ and $4n$ reaction channels were comparably more suppressed.

The abundance of the different hafnium isotopes in the target wheel and corresponding possible EVRs, produced in the $3n$ evaporation channel for the two beam projectiles, are displayed below in Table 1. One should expect EVRs – and their decay chains – not only corresponding to the abundance of the hafnium isotope but also to their production cross-section.

Table 1: The evaporation residues for the $3n$ evaporation channel for each of the Hf isotopes present in the $^{\mathrm{nat.}}$Hf target wheel. The data is given such that the Hf isotope of highest abundance on the left to the lowest abundance on the right. The beam ion corresponding to the EVR produced is indicated in the brackets next to 'EVR'.

Target Composition	^{180}Hf	^{178}Hf	^{177}Hf	^{179}Hf	^{176}Hf	^{174}Hf
Abundance [%]	35.1	27.3	18.6	13.6	5.2	0.2
EVR (^{48}Ca)	^{225}U	^{223}U	^{222}U	^{224}U	^{221}U	^{219}U
EVR (^{50}Ti)	^{227}Pu	^{225}Pu	^{224}Pu	^{226}Pu	^{223}Pu	^{221}Pu

The data recorded for the ^{48}Ca on $^{\mathrm{nat.}}$Hf run in 2019 was the primary focus of analysis due to its comparably larger volume to the data recorded for the ^{50}Ti on $^{\mathrm{nat.}}$Hf run in 2020 which underwent over a much shorter period. The file size of the recorded data corresponds to how often a trigger event was observed that should be proportional to production cross-sections. The ratio of the file size for the 2019 run to that of the 2020 run was $4.1\,\mathrm{GB}/1.4\,\mathrm{GB} \approx 3$.
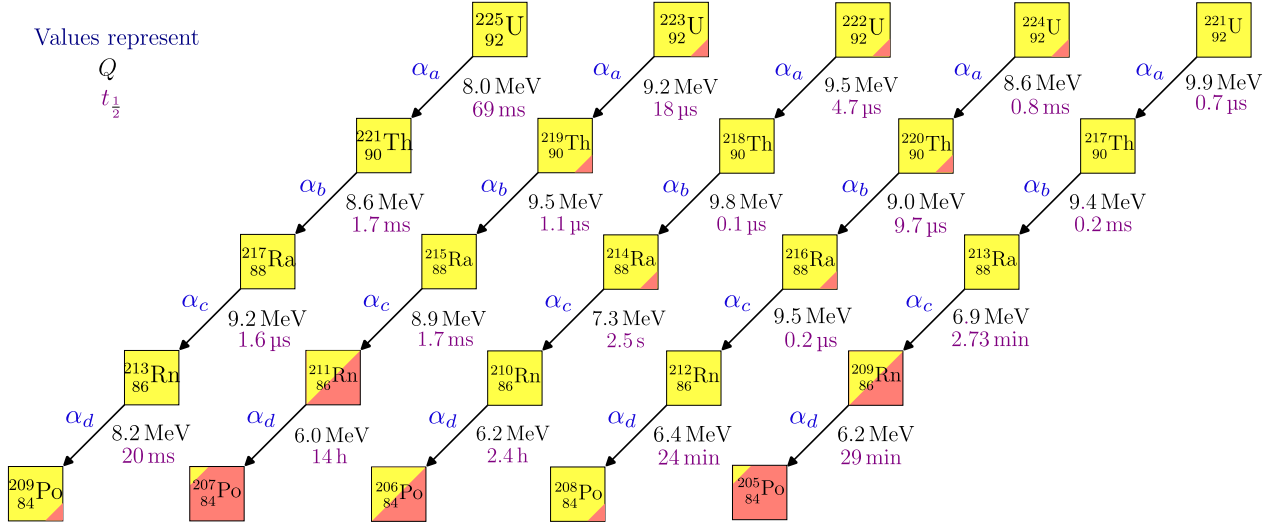

Figure 14: The decay chains of the uranium isotopes, ^{225}U-^{221}U, that could be produced during the ^{48}Ca + $^{\mathrm{nat.}}$Hf fusion-evaporation reactions. The Q-values (in black) and the half-lives (in magenta) are given next to the α-decay arrows. The yellow colour indicates alpha decay while the peach pink colour indicates beta-minus decay. The values are taken from NuDat 3.0 database in NNDC [2].

The ^{48}Ca on $^{\mathrm{nat.}}$Hf dataset is expected to produce uranium isotopes in the region of $A = 219$ to $A = 225$. The decay schemes for these uranium isotopes using existing tabulated values of α-decay energies and lifetimes – retrieved from nuclear datasheets [2]– are presented in

Fig. 14. In the figure, the chains have been truncated to only include the decays with small enough half-lives that are more likely within the time frame of our experiment. This limited any speculated decay chain to four or fewer α decays.

The Go4 correlation analysis step was run using different search parameters – mainly event energies and time – to optimise their outcome as well as obtain further informative results iteratively with the results observed in each preceding run. The 'tab-separated values' files produced were converted into pandas dataframes in Python which were then analysed. Initially, searches for general α-decay chains were performed using rather broad energy and time search criteria such that as many α-α coincidences as possible could be retrieved and observed for regions of concentrated energy peaks that could later be gated on to catch more specific chains. Table 2 shows the latest search parameters used for this first kind of general α-decay chain search. Furthermore, to keep the chain information retrieved as clean as possible, the α decays were first searched for only during the beam-off periods. EVR implantation event energies in the range of 11 to 20 MeV, and α-decay energies in the range of 5 to 10 MeV – typical values for α decays – were used in the search. The search time for every new α-decay event was set to 5 s which was deemed sufficiently long enough to catch the expected fast α-decays. In the α-decay chains of the uranium isotopes displayed in Fig. 14, it can be seen that the isotope with the longest α decay has a half-life of just 3 s. Moreover, the beam shutoff routine was not used here so it is highly likely a chain would be interrupted by a new EVR implantation event in longer searches. This would mean that correlated events would not necessarily correspond to the same decay chain.

Table 2: The search parameters used in the Go4 correlation analysis for the first general α-decay chain search.

Parameter \Event	EVR	α_a	α_b	α_c
Energy beam-on [MeV]	[11, 20]	-	-	-
Time beam-on [s]	-	-	-	-
Energy beam-off [MeV]	-	[5, 10]	[5, 10]	[5, 10]
Time beam-off [s]	-	[0, 5]	[0, 5]	[0, 5]

The extracted chains that start with an EVR implantation, *ImpA* chains, and those that start with an α_a event, *AA* chains, were separated into two distinct pandas data frames in order to analyse them independently. Histograms of the different α-event energies, energy-time plots for the α decays, and coincident α-α energy plots were created. Individually, these plots give limited information but when all of them are compared together, correlations can be observed that allow the identification of interesting energy regions that could be connected to build α-decay schemes. Moreover, histogram plots of the prompt γ-photons as well as α-γ coincidence plots were made which allowed us to spot any branching in the α decays which could be related to excited states in the daughter nuclei. One should also note that since the energy range of the α_a, α_b and α_c are equivalent in this general energy search, the α_b event would also satisfy the α_a event restarting the *AA* chain during the correlation analysis. As a consequence, the *AA* chains are limited to two α decays, [α_a, α_b], but this means the E_a-E_b plot would show all the coincident α-decays. Comparing the regions of emerging peaks in

this energy-energy plot with those found in the energy-energy plots for the *ImpA* chains, the sequence of these α decays and hence a more complete decay chain could be determined.

Afterwards, using the interesting α-decay energies obtained in the first general α-decay chain searches, the Go4 correlation analysis was run to gate into specific chains. The average energies of the interesting α-decays were determined by averaging the counts over a localised region around each energy peak. This proved more effective than fitting a Gaussian to an energy peak and taking its amplitude since the counts were rather low making it difficult to properly fit a Gaussian. The search parameters for the first gated α-decay chain – which appeared to correspond to the ^{225}U chain as we will see in the results – are presented in Table 3.

Table 3: The search parameters for the correlation analysis step gated to specific α-decays found in the general search. The parameters which are blue indicate that those were additionally used in the search where α_a was set in the parameters for 'EVR implantation'.

Parameter \Event	EVR	α_a	α_b	α_c	α_d
Energy beam-on [MeV]	[11, 20]	[7.85, 7.95]	-	-	-
Time beam-on [s]	-	-	-	-	-
Energy beam-off [MeV]	-	[7.85, 7.95]	[8.15, 8.55]	[9.01, 9.07]	[8.10-8.20]
Time beam-off [s]	-	[0, 5]	[0, 5]	[0, 5]	[0, 5]

As before, the α decays were only searched during beam-off periods. Additionally, to get energies of a fourth α decay within the chains, further correlation analysis runs where the α_a event was used as an 'EVR implantation', and so would only be seen during beam-on periods, were performed. The same type of plots that were produced during the general search were produced and analysed. Furthermore, the half-lives of the observed α-decays were estimated by plotting counts of event times for energies gated to the α decays and fitting an exponential decay curve. The exponential decay equation that relates the counts $N(t)$ at time t to the decay constant λ is

$$N(t) = N(0)e^{-\frac{\lambda t}{\tau}}. \tag{11}$$

The relations to convert between the decay constant λ, lifetime τ, and half-life $t_{\frac{1}{2}}$ is

$$t_{\frac{1}{2}} = \tau \ln 2. \tag{12}$$

Searching for different α-decay chains using α-events during only beam-off periods, albeit giving clean chains, proved to be a challenging task on account of the α decays in most of the chains having half-lives in the microsecond or lower range, meaning these fast α emissions would have a high probability to occur during the beam-on periods, thus resulting in successfully hunting them very rarely if at all. As a consequence, a better methodology to extract the fast α emissions from the beam-on periods while also having high confidence when assigning them to specific decay chains had to be devised. To search for clean fast α-decay events, a second general α-decay chain search but with the last two, α_b and α_c, events being observed during beam-off periods while the first α_a being observed during either beam-on or beam-off periods. The search parameters used are displayed in Table 4. Again,

the same plots as the first general search were produced and analysed. During the analysis, it was attempted to find energy peaks that emerged during the beam-off periods that could be gated to distinct energy peaks in the beam-on periods. Using the results found, further correlation analysis runs using any two distinct correlated α-α energy peaks as gates, i.e. E_b and E_c, for the search. In these searches, the first two – α_a and α_b – events would be searched for during both beam-on and beam-off periods, while the last α_c searched for during only beam-off periods. The extracted $ImpA$ and AA chains were then analysed in the same way as before.

Table 4: The search parameters used in the Go4 correlation analysis for the second general α-decay chain search.

Parameter \Event	EVR	α_a	α_b	α_c
Energy beam-on [MeV]	[11, 20]	[5, 10]	-	-
Time beam-on [s]	-	[0, 5]	-	-
Energy beam-off [MeV]	-	[5, 10]	[5, 10]	[5, 10]
Time beam-off [s]	-	[0, 5]	[0, 5]	[0, 5]

4.3   α-Decay Energy Corrections

Two main energy corrections need to be considered to accurately determine the energy of the observed α decays. Both corrections adjust for the reduction in the detected energy of an α decay. One is to take into account the reduction due to the plasma effect, and the other is to correct for energy deposited in the charge-insensitive layer of the DSSD strips. Let us consider the plasma effect first. The energy deposited in the silicon detectors during an α decay should be the sum of the kinetic energies of the α particle and the recoil nucleus, i.e. the Q_α value. However, the detected energy is slightly reduced owing to the massive recoil nucleus for which only a fraction of the very locally deposited kinetic energy is measured by the detectors as a result of possible electron-hole recombination. The kinetic energy of the recoil nucleus induces the creation of an enormous amount of electron-hole pairs – which act as charge carriers – but over a very short distance. The locally-strong electric field from this dense region of electron-hole pairs counteracts the electric field from the applied reverse bias resulting in an overall weaker electric field that impedes charge collection. The charge collection is delayed by a so-called plasma time. The weaker electric field results in a higher probability of recombination of the electron-hole pairs that were created. Loss of the information carriers means that the final collected charge and hence the detected energy is reduced. The plasma effect depends on the Z value of the recoil nucleus, as well as the charge collection efficiency of the detectors. To correct for the plasma effect, the recoil fraction r was determined. The relation between the detected energy E_{det} and actual α-decay energy E_α for a recoil nucleus of mass number A is given by

$$E_{det} = E_\alpha \left(1 + \frac{4}{A-4} r \right). \tag{13}$$

This relation was used to calculate r using measured E_{det} and tabulated E_α for well-known α emitters during the calibration stages. These included α emissions from ^{252,253}No and ^{248}Fm

from ^{48}Ca + ^{206,207}Pb reactions as well as other $A \approx 220$ transfer reaction products during the main experiment. A Z^2 dependence on r was determined by performing a logarithmic least-square fit to the data. The fit parameters can be used to determine r for different Z. Plot showing how r, using the calculated fit parameters, varies with Z is presented in Fig. 15. The plot with the actual experimental data and fitting is available in Ref. [22]. For the isotopes investigated in this thesis work, r is around 0.40 to 0.45. Using the r value, one can retrieve the actual E_α and, in turn, Q_α using Eqn. 3 or vice versa to calculate what E_{det} one should expect for an known Q_α of an isotope.
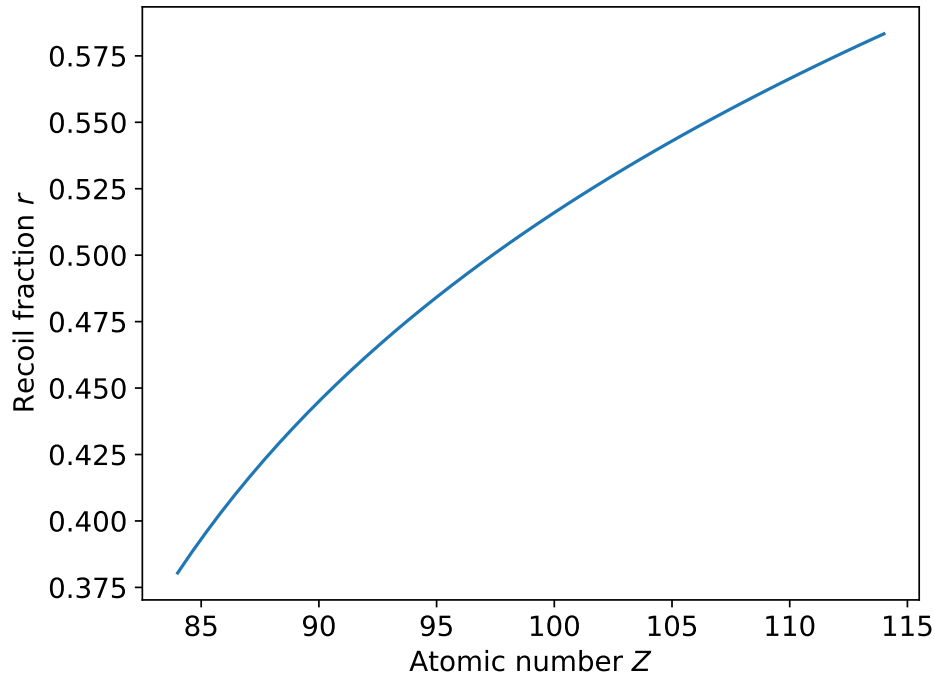
Figure 15: Variation of the recoil fraction – obtained using calculated fit parameters – with Z.

The second energy correction that one needs to perform is when reconstructing the full energy of an α particle that ended up in the BOX DSSD after escaping the IMP DSSD. The DSSDs have a layer of SiO_2 which is charge-insensitive and where no energy can be detected from ionising radiation. The thickness of this so-called 'dead layer' varies pixel-by-pixel. Figure 16 illustrates the scheme of an α-decay event where the full energy is retrieved by reconstruction. One needs to correct for energy losses in the dead layers of both the IMP DSSD pixel and the BOX DSSD pixel that an α particle traverses. It is also necessary to include the angle dependencies between the IMP DSSD pixel and the BOX DSSD pixel. This is achieved using geometrical factors g_f and the implantation depth d in the IMP DSSD. The track length in the dead layers and stopping powers of α particles in SiO_2 at different energies are used to determine the required energy correction.
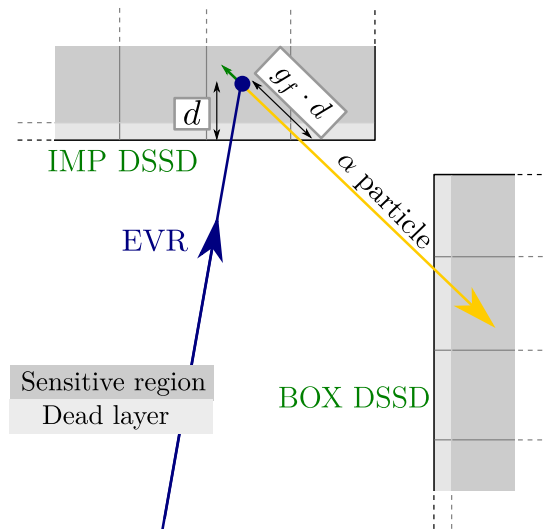
Figure 16: Illustration of an α-decay event that requires energy reconstruction and the relevant parameters that are required. Image modified from Ref. [1].

The pixel-by-pixel dead layer thicknesses were determined during the detector characterisation stage of the DSSDs. The relation between the actual α-particle energy and the dead layer correction was investigated using the known α-particle energy of 8.40 MeV from ^{252}No produced in the ^{206}Pb + ^{48}Ca fusion-evaporation reaction [1]. Since the initial energy of the α particle was known, it could be used to determine d using SRIM calculations based on the Bethe-Bloch relation [31]. A visible correlation between the implantation depth d and EVR energy was observed. As a consequence, all the necessary information is available to determine the dead layer corrections because the dead layer penetration – as a function of the observed α-particle energies, geometrical factors, and implantation depth – could be coupled to the full reconstructed α-particle energy. Further details on α-energy reconstruction and DSSD dead layers can be found in Refs. [1, 23].

4.4   Prompt α-γ Coincidences

The energies deposited in the Ge detectors are recorded for about 5 μs once a trigger is accepted, but to evaluate the fine structure of the α decays, it is only the γ photons registered in prompt coincidence with an α decay that are of relevance. The γ-energy distribution with γ photons emitted at a trigger time t_{trig} has a characteristic 'banana' shape as displayed in Fig. 17(a) and Fig. 18. Low energy γ photons reach shallower depths and the collection of their information carriers can take longer to reach the energy collection point in the Ge crystals resulting in a wider time spread. As the energy increases, the interaction points are deeper and correspondingly their information collection is faster therefore closer in time to the trigger time. Low energy γ photons below 50 keV may not reach the crystals due to the aluminium casing of the detector or their signals may be too low such that it becomes difficult to separate them from electronic noise. High energy γ photons in the MeV range have greater penetration and become less likely to interact with the detector. The size of the banana shape is dependent on the Ge crystal, including its type, size, shape, and width. The

Compex Ge crystals used in our experiment have 'only' 5 cm depth and are not optimised for the detection of photons in the order of MeV.
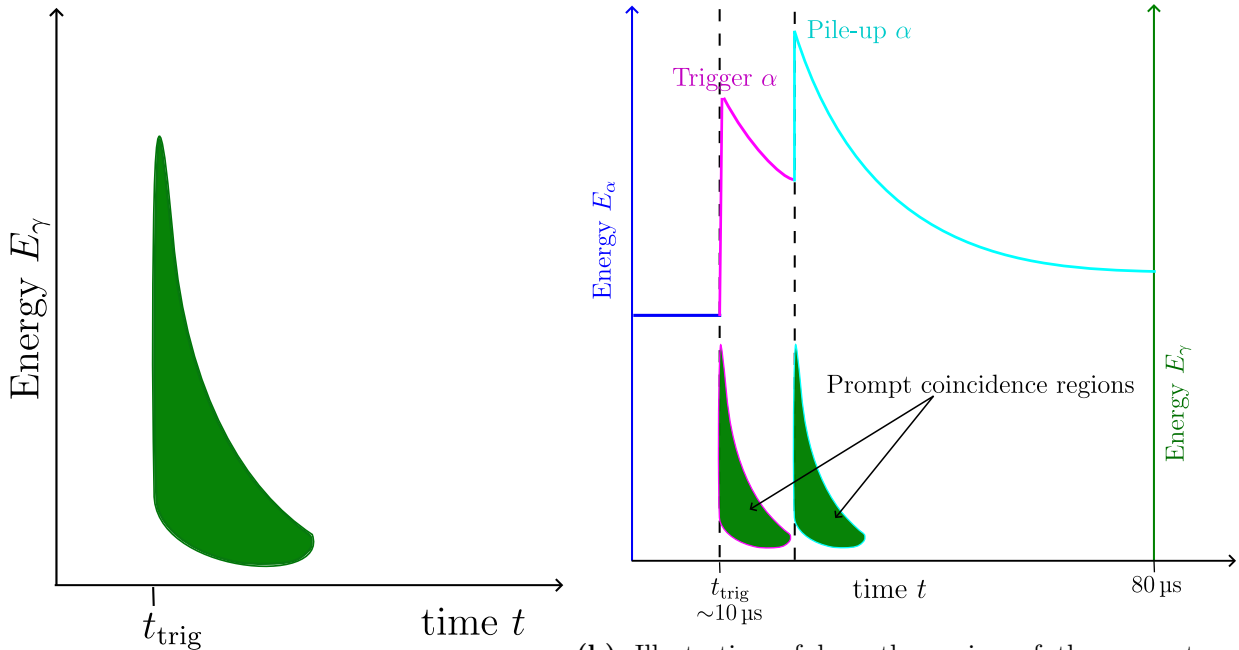
(a) The expected banana plot for prompt γ photons following a trigger.

(b) Illustration of how the region of the prompt α-γ coincidence has to vary relative to the position of the α-decay event, including the presence of pile-up events.

Figure 17: Sketches of the γ rays following a trigger and how it relates to prompt α-γ coincidence searches.

The concept of selecting γ photons that come in prompt coincidence with an α-particle emission is illustrated in Fig. 17(b). An α-decay event triggers the recording of all events in the detectors. The α decay that sets off the trigger should have one or more corresponding prompt γ-photons, if it has any, lying within the 'banana' polygon in the energy-time plot. This polygon within which the γ-photon point – i.e. (energy, time) – lies is always relative to where the α decay was registered. Most α particles which were part of the trigger scheme are naturally seen right after the trigger time in the trace and thus the prompt γ-photon would also be found around the trigger time. However, in case of pile-up events as expected in our experiment, more than one α-decay event will come in the same trace i.e. even after the trigger time and hence the prompt γ photon should be checked for and seen in a 'banana' polygon shifted to the coincident time at which the α-decay event also registered. Fig. 18 shows the prompt γ-photon distribution in time within a trace for our experiment where the banana polygon mask used is clearly visible. The relative times of the pile-up signals have been taken into account so they do not show up separately here.
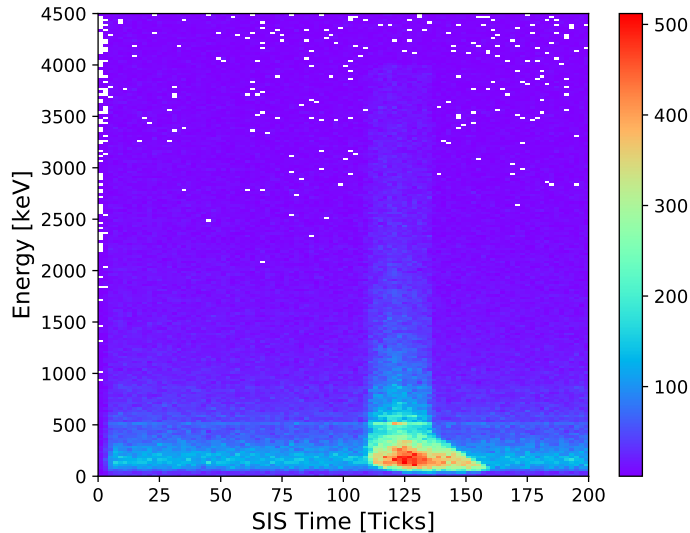
Figure 18: The banana shape of the prompt γ photons recorded following trigger is clearly visible in the experimental data of the experiment.

5   Results

The data analysis of the ^{48}Ca + $^{nat.}$Hf reaction has produced interesting results and there is the prospect that further analysis will bring more. This section presents the key findings and shows minor nuclear structure interpretations from the analysis of the extracted chains of correlated events. First, the results of the search where all correlated α decays were only picked during beam-off periods which comprised a deduced decay scheme along with strong indications of possible new α-decay fine structure. Afterwards, the results from the search where the first α, i.e. α_a, was picked during either beam-on or beam-off periods with the rest of the α only during beam-off. Finally, some discussion of spectra that showcase the new fine structure of the α decay into ^{217}Ra.

5.1   Searches of α during Beam-off-only Periods

The start of the chain hunt of the α decays involved the general search for all correlated α decays from which the main decay chain found corresponded to the $^{225}_{90}$U isotope. The plots of the detected α-decay energies, E_{det}, for the first three correlated α decays starting with an EVR implantation, i.e. the $ImpA$ chains, are presented in Fig. 19. The corresponding energy-time correlation plots are presented in Fig. 20. From these initial results, the full energy peaks of α decays present were obtained and determined how far in the decay chain they could be expected.
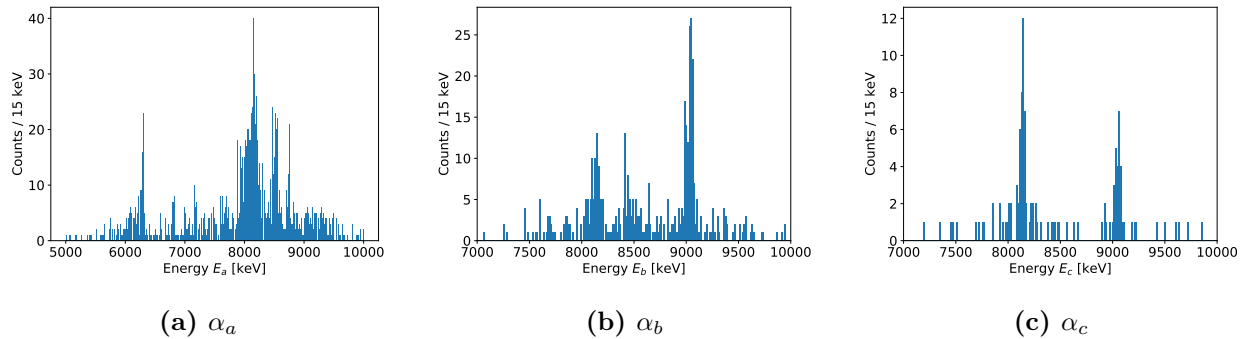
30

(a) α_a **(b)** α_b **(c)** α_c

Figure 19: The detected energies, E_{det}, of the three α-decay events following an EVR implantation event obtained in the general search.

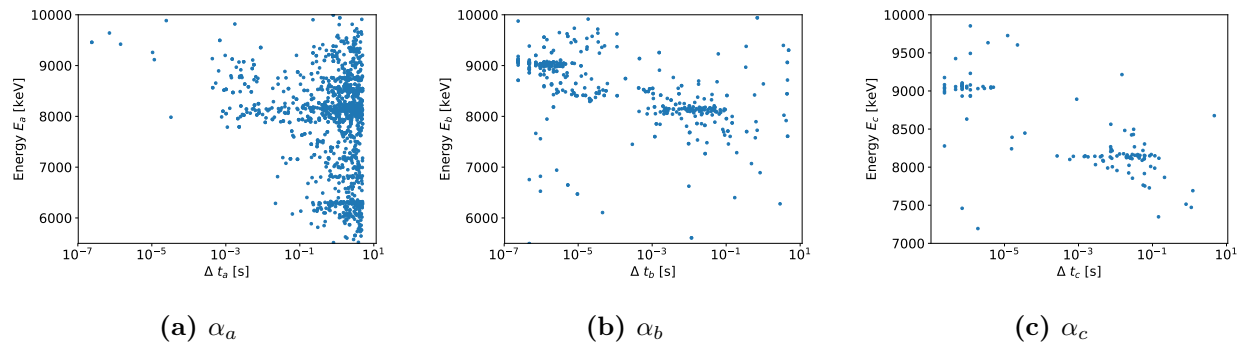**(a)** α_a **(b)** α_b **(c)** α_c

Figure 20: Energy-time correlations between the α-decay energies and time following an EVR implantation event obtained in the general search.

Next, to determine the main correlated α decays, i.e. not random correlations, the energy-energy correlations were plotted. The energy-energy coincidence plot for all the correlated α-decays is presented in Fig. 21(a) along with the times between the two α-decay events in Fig. 21(b). Combining the information from all the different plots, it can be seen that an α decay with detected energy of 9.05(2) MeV came in coincidence with three other α decays – two before, with energies of 8.20(2) MeV and 8.52(2) MeV, and one after with energy of 8.15(2) MeV. Thus, it was possible to deduce a decay chain with a length of three α decays, including a branching in one of them.
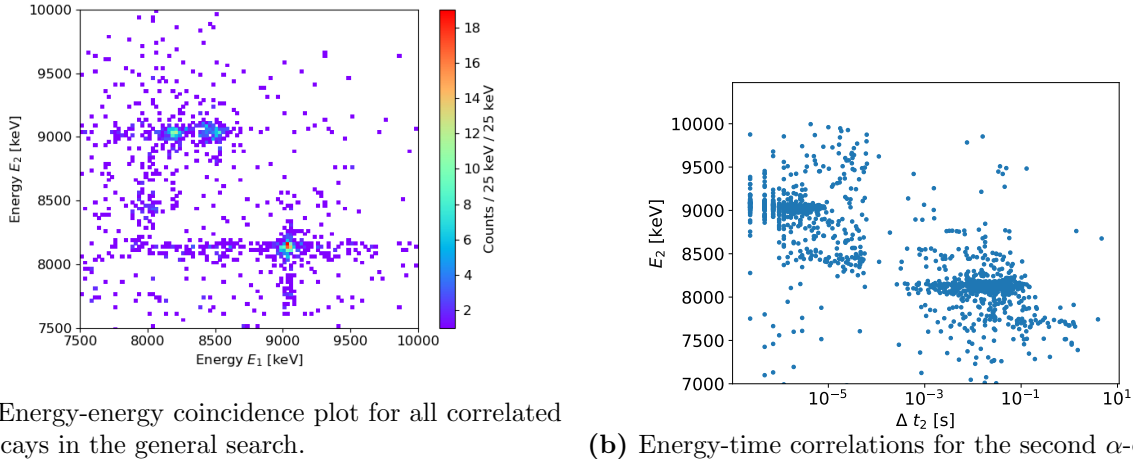
(a) Energy-energy coincidence plot for all correlated α-decays in the general search.

(b) Energy-time correlations for the second α-decay.

Figure 21: All the α-α coincidences present in the general search and the decay times for the second α-decay event.

Next, to ensure that branching in the decay path was certainly seen, the coincidences of the α-decays with the prompt γ photons were investigated. This α-γ coincidence plot for the α-decays corresponding to the energies E_1 in Fig. 21(a), where the branching is seen, is displayed in Fig 22(a). Additionally, the spectra for all the γ-photon energies in prompt coincidence with an α-decay is shown in Fig. 22(b). It could be seen that there is a comparatively very intense γ ray of 330(5) keV is present, and this is in coincidence with mainly the smaller of the two α-decay energies that were hypothesised to be branches from the same parent nuclei. Furthermore, the total of the smaller α-decay energy and the γ-ray energy adds up to the higher α-decay energy. This confirms the observation of fine structure in the α decay.
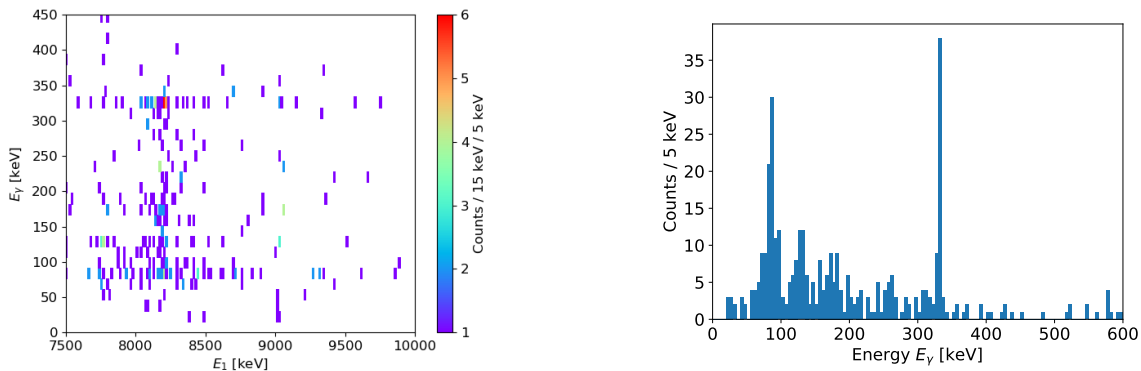
**(a)** The α-γ coincidence plot for the E_1 α-decays in previous figure.

(b) The spectrum for γ photons in prompt coincidence.

Figure 22: Plots concerning α-γ coincidences in the general search.

## ^{225}U Decay Scheme and Fine Structure of α Decay to ^{217}Ra

Following the general search, a gated search on the ^{225}U α-decay chain was performed for verification. It was noted that in general the decay path including the energies matched

rather well with the tabulated ones. The measured energy spectra of the α decays from the four steps in the decay chain along with the half-lives of the decays are presented in Figs. 23 to 26 following the step notation introduced in Fig. 13. New results on the 'b' step of the decay chain will be discussed below.
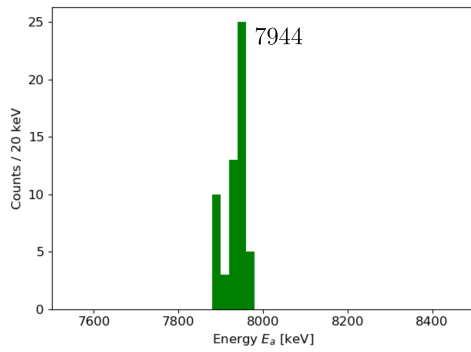
(a) The α_a energy.
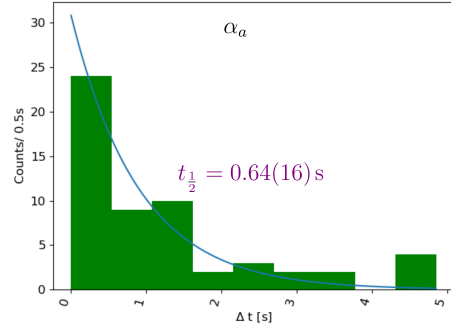
(b) Decay curve, and its fit, for half-life determination.

Figure 23: Experimentally determined quantities for the 'a' step of the decay chain.
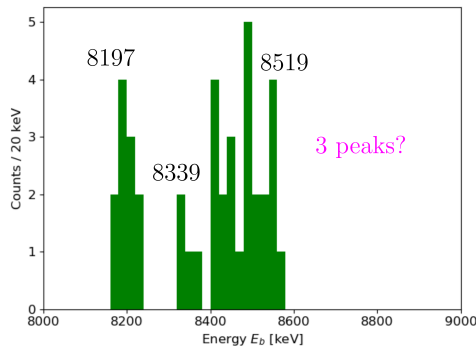
(a) The α_b energy.
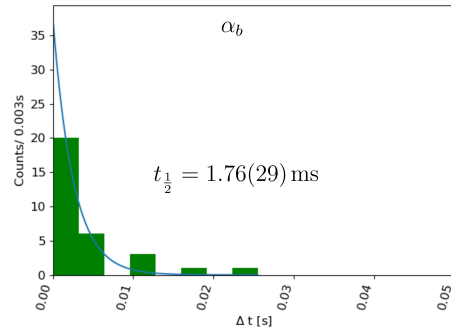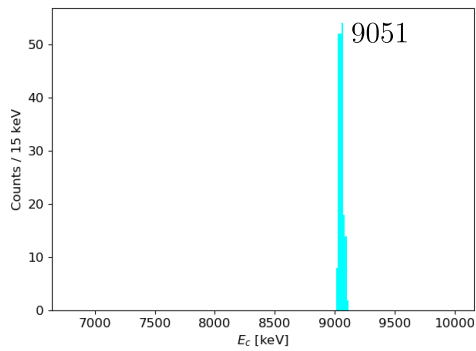
(b) Decay curve, and its fit, for half-life determination.

Figure 24: Experimentally determined quantities for the 'b' step of the decay chain.

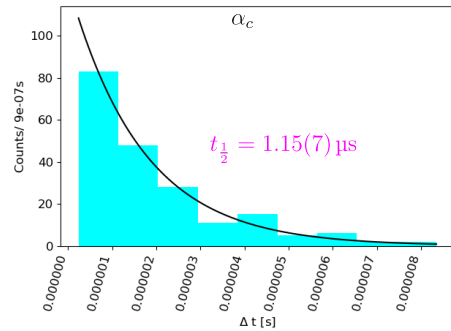**(a)** The α_c energy.

(b) Decay curve, and its fit, for half-life determination.

Figure 25: Experimentally determined quantities for the 'c' step of the decay chain. The half-life is given in pink colour to highlight that the determined value is different from the tabulated one.
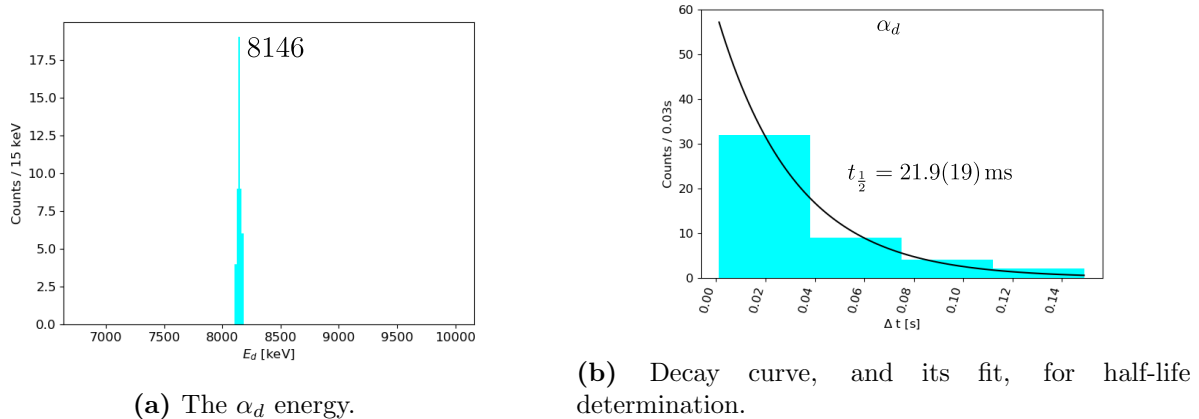
(a) The α_d energy.

(b) Decay curve, and its fit, for half-life determination.

Figure 26: Experimentally determined quantities for the 'd' step of the decay chain.

For the determination of the α-decay half-lives, the choice of choosing the correct bin size for the time was very critical and affected the value obtained dramatically. The bin size was adjusted until a satisfactory fit was obtained by judging how well the data was fitted by eye along with the best reduction of the fit uncertainty. Among these results, of particular interest were the spectra for the α_b decay where three, maybe four, energy peaks rather than the expected number of two were observed. Additionally, the half-life of the α_c decay was determined to be $1.15(7)\,\mu$s which is smaller than the current tabulated half-life of $1.6\,\mu$s. The use of digitised preamplifier signals and a relatively good number of counts for the half-life determination could mean this discrepancy likely is an improved value obtained. Moreover, the other half-lives obtained agreed well with tabulated values – except the α_a decay but this could be explained by the interruptions of many $ImpA$ chains by succeeding implantation events during beam-on before the α_a was detected resulting in an underestimation of the α_a half-life. Finally, the α_b-γ coincidence plot and the prompt γ spectra are shown in Fig 27. Here, it was confirmed that a 333-keV γ came in prompt coincidence exclusively with the 8.2-MeV α_b event. Moreover, prompt photons of about 210 keV and 225 keV of comparable counts to the 333-keV γ photon are seen which hint at new α-decay fine structure. The tentative fine structure of the α decay to ^{217}Ra that is inferred from the α_b-γ coincidence plot is displayed in Fig. 28.
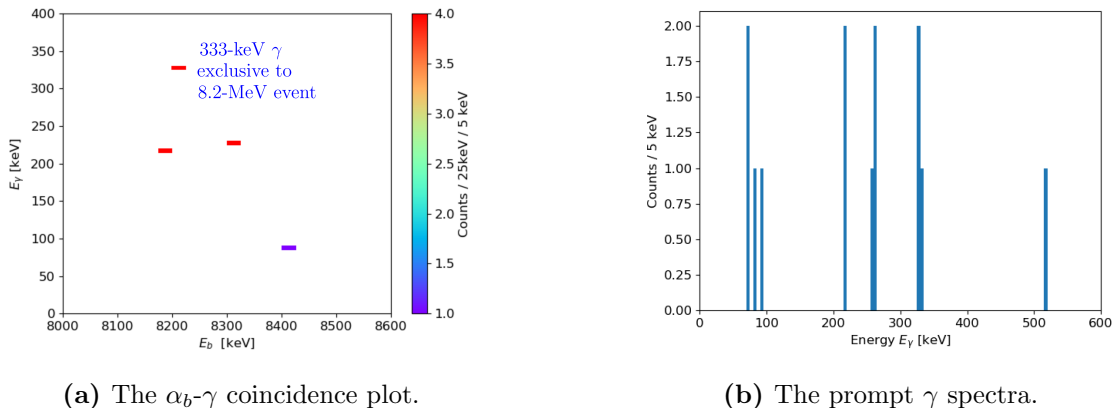

(a) The α_b-γ coincidence plot.

(b) The prompt γ spectra.

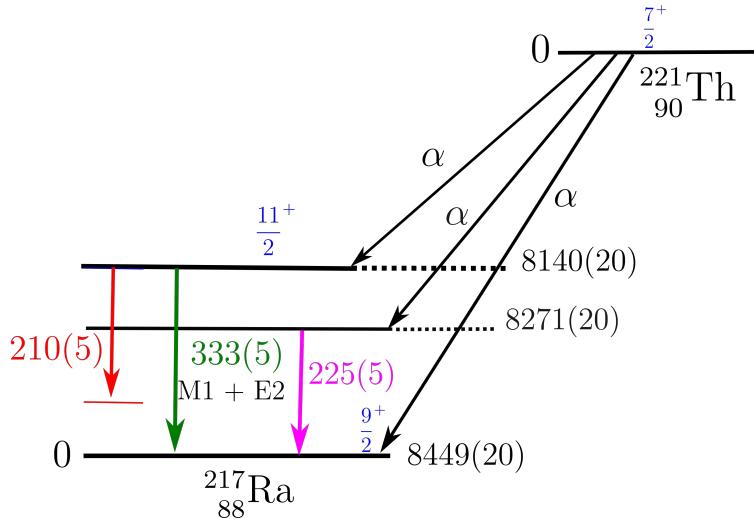**Figure 27:** Checking for fine structure of ^{221}Th α decay.

Figure 28: The observed fine structure of α-decay to ^{217}Ra. The full energies of the α particles are given taking into account the recoil fraction correction on the detected energies. All energies are in keV. The tabulated spin-parity assignments of known levels are shown in blue.

In the fine structure diagram, ^{221}Th decays to ^{217}Ra through three different α-decay modes. The 8271-keV α decay is followed by a 225-keV γ-ray in prompt coincidence. The energies of the α decay and the γ ray add up to the 8449-keV α decay within the experimental uncertainties. This decay mode has not been reported earlier and would be its first observation once verified. The 333-keV γ ray follows the 8140-keV α decay as expected. On the other hand, the 210-keV γ ray also follows the 8140-keV α decay but it is about 120 keV short of reaching the lower energy level. The nuclear state from which the 210-keV γ ray comes is tentative. Assuming it starts at the same nuclear state as the 333-keV γ ray, it could have resulted in a low excited state in the ^{217}Ra that is just above the known ground state and de-excites mainly through internal conversion. This would require searches for coincident conversion electrons in the BOX DSSDs. The opposite scenario is also possible where it follows after a nuclear de-excitation of 120 keV. The 333-keV γ ray is from M1 or E2 transition according to selection rules. The 210-keV and 225-keV γ ray transitions are likely to be of this type although the nuclear structure of the initial and final states they are transitioning through needs to be explained. Further analysis is necessary to verify the presence of these possible two states that correspond to the 210-keV and 225-keV γ ray transitions. These states come with the α decays from the ^{221}Th nuclei, and it has been previously reported but not confirmed of a γ-ray peak at 208 keV. Hence, our result can further strengthen the case of the 210-keV γ puzzle after more stringent data analysis.

The final decay chain and the decay level scheme that could be constructed are given in Fig. 29. The detected energies, E_{det}, were converted into α-decay energies, E_α, using the recoil fraction correction for ^{225}U. The energy values and half-lives for most of the decays agree with the current tabulated values. Possible new findings are highlighted using blue circles. The 210-keV γ puzzle is highlighted in red.
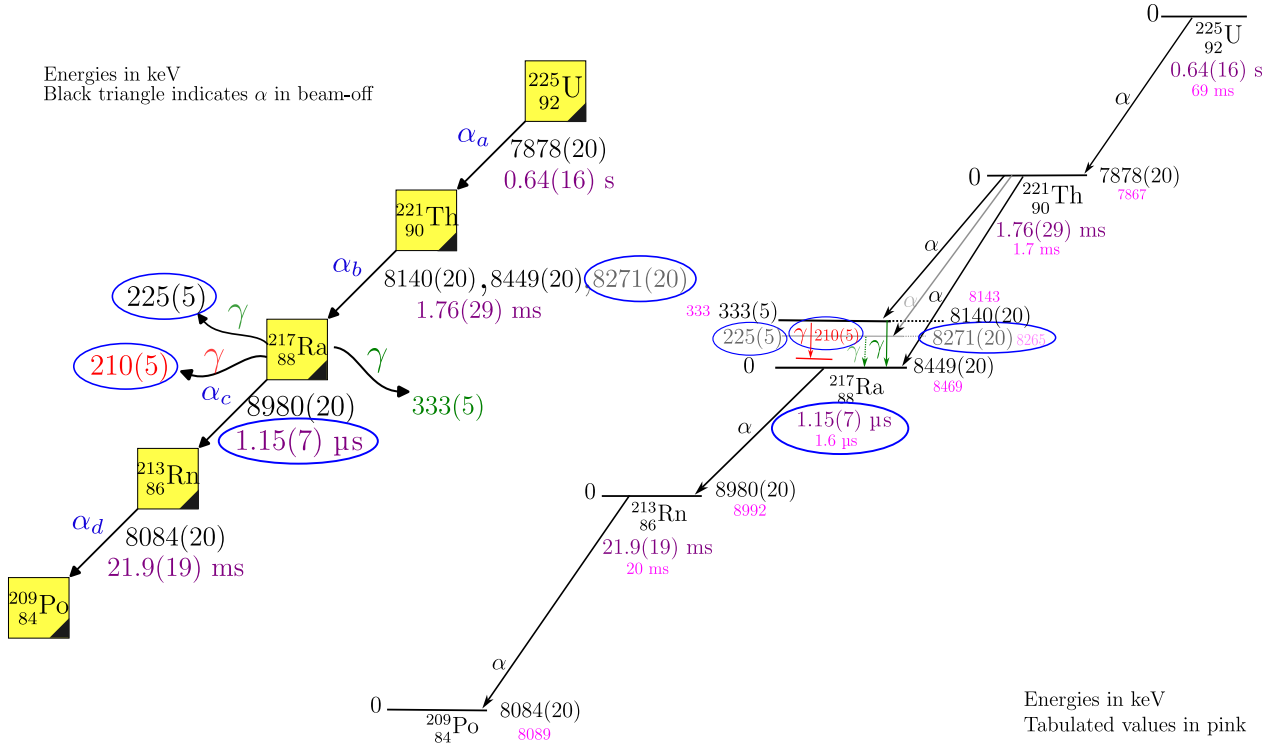
Figure 29:   The deduced decay paths and the decay modes for the ^{225}U isotope from the experimental data. On the left, the decay chain is shown. All four of the α decays in the ^{225}U decay chain were deduced from the experimental data. On the right, the observed decay scheme showing the full kinetic energies of the α particles and the branching in the ^{221}Th decays. The calculated half-lives are also given next to their respective nuclei. Results of interest which indicate new findings are emphasised using blue circles. The state involving the 210-keV γ puzzle is highlighted in red.

5.2   Searches with α_a in Beam-on/off Periods

The next step going from the α decay searches during only beam-off to the data analysis to pick out the fast α decays coming during either beam-on or beam-off was attempted. The energy-energy correlation plot – from the AA chain – of this second general α search is presented in Fig. 30(a). An extra energy-energy correlation peak at $(E_1,\ E_2) \approx (8.7, 9.4)$ MeV can be observed in addition to the correlation peaks already observed during the beam-off only searches. Several more energy peaks are observed in the individual α spectra as well. The most intense of these new α peaks, 8.76 MeV, in the α_2 spectra of the AA chain – which is during beam-off – was gated to determine the correlating α_1 peak that is during either beam-on or beam-off (see Fig. 30(b)). The gated α_1 spectra shows a clear peak at 9.42 MeV as shown in Fig. 31(a). The corresponding fitted decay curve for determination of the half-life is displayed in Fig. 31(b). Since the number of counts used for the fit was not very high, the determined half-life was not expected to be accurate (and is overestimated compared to the tabulated value). The decay chain from these two correlated α decays which matches with part of the $^{223}_{92}$U decay chain is presented in Fig. 32.
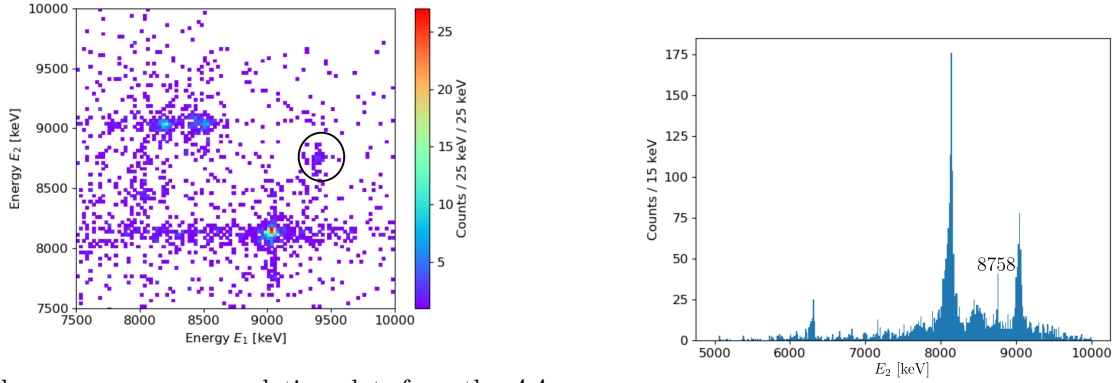
(a) The energy-energy correlation plots from the AA chain. The new correlation peak seen is highlighted with the black circle.

(b) The energy spectra of the second α decay in the AA chain.

Figure 30: Energy plots for α-decay events for the second general search.
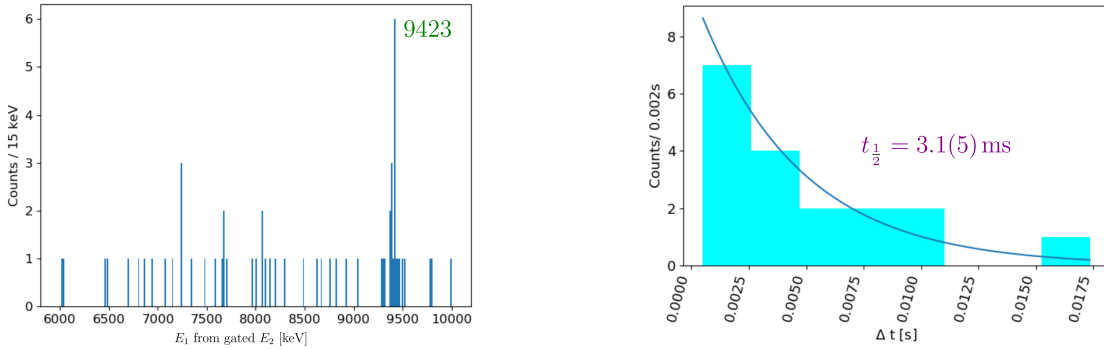
(a) The α_1 energy peak from gating on the 8758-keV α_2 energy peak.

(b) The fitted decay curve for half-life determination of the 8758-keV α_2 decay.

Figure 31: Gated spectrum of α_1 and the half-life determination of the 8758-keV α decay.

Energies in keV
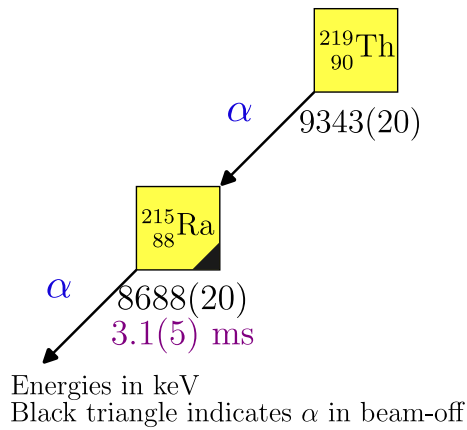Black triangle indicates α in beam-off

Figure 32: The decay chain of fast α decays deduced that is part of $^{223}_{92}$U decay chain. The full energies of the α particles are given taking into account the recoil fraction correction on the detected energies.

5.3 Hints of New Fine Structure of α Decays

The γ-ray spectra and the α-γ coincidence plots from different searches appear to contain information that hints at new fine structure of α decay for a handful of the isotopes in our study. A collection of these plots is presented in Fig. 33.
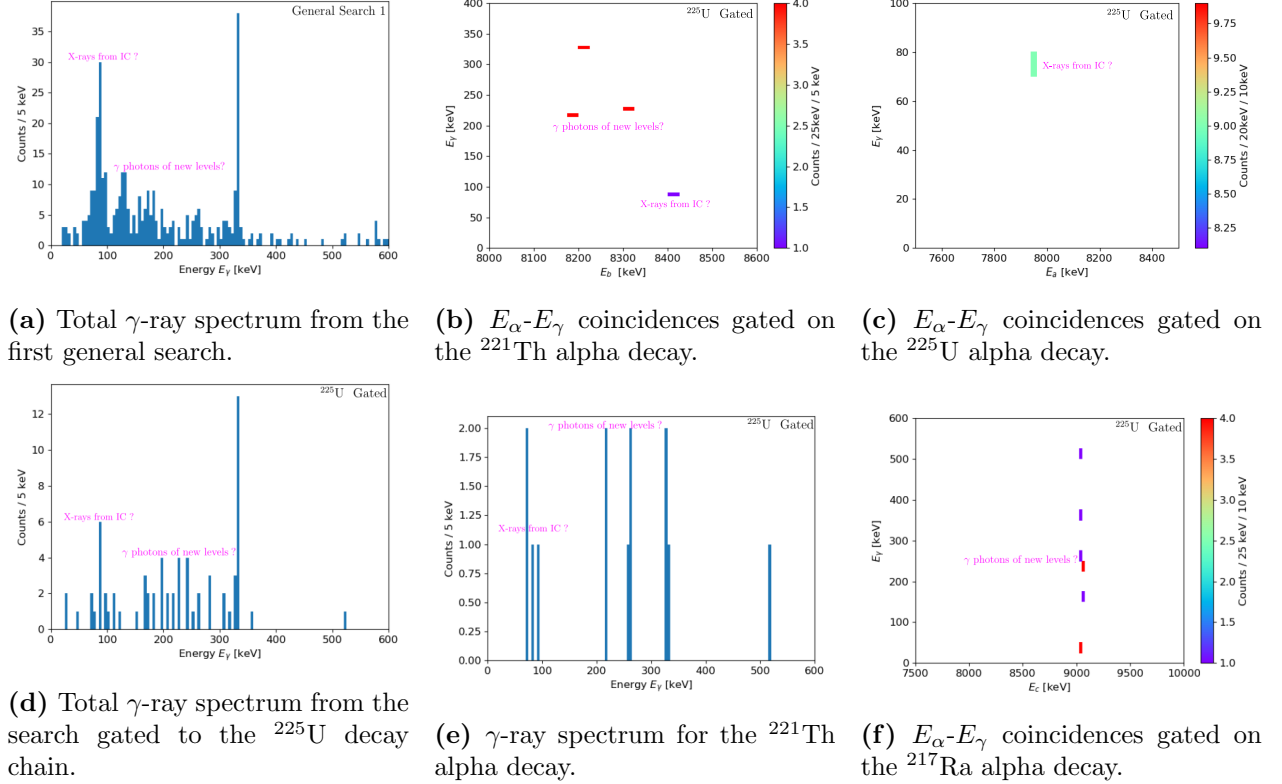

(a) Total γ-ray spectrum from the first general search.

(b) E_α-E_γ coincidences gated on the ^{221}Th alpha decay.

(c) E_α-E_γ coincidences gated on the ^{225}U alpha decay.

(d) Total γ-ray spectrum from the search gated to the ^{225}U decay chain.

(e) γ-ray spectrum for the ^{221}Th alpha decay.

(f) E_α-E_γ coincidences gated on the ^{217}Ra alpha decay.

Figure 33: γ spectra and α-γ coincidence plots from different searches that could hint at new fine structure of α decay.

In Fig. 33(a), there are additional distinct peaks at about $84\,\text{keV}$, $130\,\text{keV}$, $170\,\text{keV}$, $210\,\text{keV}$, and $250\,\text{keV}$. These peaks could be from excited states resulting from decays in the chains stemming from other uranium isotopes; in particular, the $84\,\text{keV}$ photon has a comparatively high intensity. Compared with tabulated X-ray photons having congruent values, there is a possibility that this photon comes from internal conversion in the radium nuclei, although strict gating on alpha particles seems to suggest they do not come in coincidence and further analysis needs to be done to understand the nature of this peak. The Ge detectors have good energy resolution capable of resolving energies different by less than $2\,\text{keV}$ [1]. Hence, the photon energy should be quite accurate and if it is indeed an X ray, this would imply the presence of a new highly converted excited state. Similarly, prompt photons can be seen in the α-photon coincidence plots for the gated search (Fig. 33(b), (c), (e), and (f)). When gating on the parent decay, a hint for new excited states corresponding to γ photons of about $210\,\text{keV}$, $225\,\text{keV}$, and possibly X-ray photons around $90\,\text{keV}$ for ^{217}Ra can be seen in 33(b). The $75\,\text{keV}$ photons in prompt coincidence with α_a decays from the gated search (shown in Fig. 33(c)) could be X rays from internal conversion in ^{221}Th. Few counts of photons of

different energies are seen in prompt coincidence with the α_c decay (corresponding to ^{213}Rn daughter nuclei) in Fig. 33(f). Finally, several peaks are seen in the γ spectra from the gated search shown in Fig. 33(e). All these photons from the different plots require a deeper investigation and comparison with `GEANT4` simulations.

6   Conclusion & Outlook

Through a comprehensive data analysis of the scarce recorded experimental data, two α-decay chains were clearly identified and studied. It was possible to recreate the main anticipated α-decay chain from the ^{225}U isotope. There are clear indications of fine structure in α decay within the chain as well as a new half-life value for ^{217}Ra. Moreover, one of the fast α decays, in the order of sub-microseconds, of the other uranium isotopes which are expected to come during beam-on periods could be observed as well.

The next steps concerning this dataset would be to perform further dedicated analysis on the γ spectra and α-γ coincidences. These already hint at new excited states. Depending on whether the prompt photons observed are determined to be γ rays or X rays following internal conversion, one can infer their likeliness to a corresponding transition type, for example, E1 for internal conversion or E2/M2 for γ transition. For the low energy photons ($< 100\,\text{keV}$), a search on the BOX DSSDs need to be performed looking for unnoticed prompt coincident conversion e^- to confirm that they are indeed X rays. `GEANT4` simulations of the experiment adjusted to produce these photons could be done and compared to our experimental results to check the likelihood of randomness in our measurements. Following this, nuclear structure interpretations such as evaluating quadrupole deformation parameter β could be carried out. One can perform one last deeper look into the beam-on data analysis and the ^{50}Ti + $^{\text{nat.}}$Hf reaction dataset as well. The results of this analysis – until now – are already interesting enough and they are suitable to be publish in a peer-review article.

For future similar experiments – such as the possible U319 rerun which probes overlapping regions of the chart of nuclides covered in this writing – a few improvements can be suggested following this study. Beam energy could be adjusted to select reactions with the highest cross-sections for specific EVR production corresponding to the desired fast alpha decay chain. A target containing one specific isotope could be used to catch more unique decay chains. Different reactants could be used such that the first α emission is slow and then followed by fast ones. This would allow more chances of detecting the α decays during beam-off periods unlike when the first α-decay is fast and comes during beam-on. This would also allow for a better beam shutoff routine allowing time for the beam shutoff to activate before the beam-on periods of the beam pulse. The beam shutoff time would also need to be shortened to the expected length of the decay chain to ensure valuable beam time is not lost. The electronics could be improved to increase the capture of prompt γ rays for α decays coming as pile-ups. The current `SIS` modules only record traces for $5\,\mu\text{s}$ following a trigger event and not for the pile-ups. In the future, `FEBEX4` digitisers are expected to replace the `SIS` modules to better catch the prompt photons coming with pile-ups. In addition, having dedicated experiments should bring more data and with improved statistics better interpretations should follow. The

dataset analysed in this work is from about two days of parasitic beam time.

To conclude, interesting results have been obtained from the analysis of the experimental data from the parasitic run of the U310 experiment including hints at new excited states, and with them, new fine structure of α decay. In particular, there are strong indications of possibly two new states as well as an improved half-life of ^{217}Ra. Building on the work done in this project is expected to lead to exciting findings that would increase our knowledge and understanding of nuclear structure of these fast α-decaying isotopes.

References

1. Såmark-Roth, A. *Spectroscopy along Decay Chains of Element 114, Flerovium* PhD thesis (2021).

2. *NuDat 3.0, NNDC Database* `https://www.nndc.bnl.gov/nudat3/` (2023/12/10).

3. Sitenko, A. & Tartakovskii, V. *Theory of Nucleus: Nuclear Structure and Nuclear Interaction* 1–90 (Springer Netherlands, 1997).

4. Bäckman, S.-O., Brown, G. E. & Niskanen, J. A. The nucleon-nucleon interaction and the nuclear many-body problem. en. *Phys. Rep.* **124,** 1–68 (July 1985).

5. Hussein, E. M. A. in *Radiation Mechanics* 1–65 (Elsevier, 2007).

6. Caurier, E., Martínez-Pinedo, G., Nowacki, F., Poves, A. & Zuker, A. P. The shell model as a unified view of nuclear structure. en. *Rev. Mod. Phys.* **77,** 427–488 (June 2005).

7. Stavsetra, L. *et al.* Independent verification of element 114 production in the ^{48}Ca+^{48}Pu Reaction. *Phys. Rev. Lett.* **103** (Sept. 2009).

8. Krane, K. S. *Introductory Nuclear Physics* 3rd ed. en, 135–138 (John Wiley & Sons, Nashville, TN, Oct. 1987).

9. L'Annunziata, M. F. in *Radioactivity* 653–665 (Elsevier, 2023).

10. Krane, K. S. *Introductory Nuclear Physics* 3rd ed. en, 246–248 (John Wiley & Sons, Nashville, TN, Oct. 1987).

11. Krane, K. S. *Introductory Nuclear Physics* 3rd ed. en, 251–255 (John Wiley & Sons, Nashville, TN, Oct. 1987).

12. Geiger, H. & Nuttall, J. The ranges of the α particles from various radioactive substances and a relation between range and period of transformation. *Philosophical Magazine* **22,** 613–621 (1911).

13. Qi, C. *et al.* On the validity of the Geiger–Nuttall alpha-decay law and its microscopic basis. *Phys. Lett. B* **734,** 203–206 (June 2014).

14. Cox, D. *et al.* Discovery and Spectroscopy of Neutron-Deficient Pu Isotopes and their Alpha-Decay Daughters. *UNILAC Proposal* (2020).

15. Gallagher Jr, C. J. & Rasmussen, J. O. Alpha-decay hindrance-factor calculations. en. *J. Inorg. Nucl. Chem.* **3,** 333–344 (Jan. 1957).

16. Krane, K. S. *Introductory Nuclear Physics* 3rd ed. en, 257–259 (John Wiley & Sons, Nashville, TN, Oct. 1987).

17. Krane, K. S. *Introductory Nuclear Physics* 3rd ed. en, 260–261 (John Wiley & Sons, Nashville, TN, Oct. 1987).

18. Krane, K. S. *Introductory Nuclear Physics* 3rd ed. en, 341–347 (John Wiley & Sons, Nashville, TN, Oct. 1987).

19. Sayed, T. *Assessment of the Capability for Vetoing Beta-Decay Events in the Lundium Decay Station* Bachelor thesis (2022).

20. Andersson, L.-L. *et al.* TASISpec—A highly efficient multi-coincidence spectrometer for nuclear structure investigations of the heaviest nuclei. en. *Nucl. Instrum. Methods Phys. Res. A* **622,** 164–170 (Oct. 2010).

21. Semchenkov, A. *et al.* The TransActinide Separator and Chemistry Apparatus (TASCA) at GSI – Optimization of ion-optical structures and magnet designs. en. *Nucl. Instrum. Methods Phys. Res. B* **266,** 4153–4161 (Oct. 2008).

22. Cox, D. M. *et al.* Spectroscopic tools applied to flerovium decay chains. *J. Phys. Conf. Ser.* **1643,** 012125 (Dec. 2020).

23. Kosta, E. *Dead layer determination for the new implantation detector of the LUNDIUM decay station* Bachelor thesis (2022).

24. Såmark-Roth, A. *et al.* Compex: a cubic germanium detector. en. *Eur. Phys. J. A* **56** (May 2020).

25. Hoffmann, J. *et al.* *GSI Report 2012-1* Scientific Report (2021).

26. Struck Innovative Systeme. *SIS3302 8 Channel 100 MS/s 16-bit ADC* `https://www.struck.de/sis3302.htm` (2023/12/07).

27. Essel, H. G. & Kurz, N. The general purpose data acquisition system MBS. *IEEE Trans. Nucl. Sci.* **47,** 337–339 (Apr. 2000).

28. Mesytec. *Detector Readout Systems* `https://www.mesytec.com/products/nuclear-physics/MSCF-16_F_V.html` (2023/12/07).

29. Såmark-Roth, A. *Extraction of energy and time from pile-up pulses with fast sampling ADC analysis techniques* Master Thesis, (2016).

30. *Go4 analysis framework* `https://www.gsi.de/en/work/research/experiment_electronics/data_processing/data_analysis` (2023/12/10).

31. Ziegler, J. F., Ziegler, M. D. & Biersack, J. P. SRIM – The stopping and range of ions in matter (2010). *Nucl. Instrum. Methods Phys. Res. B* **268,** 1818–1823 (June 2010).